Pergamon

Int. J. Solids Structures Vol. 32, No. 6/7, pp. 689–738, 1995

0020-7683/95 $9.50 + .00

0020-7683(94)00157-X

ON THE COMPRESSIVE FAILURE OF FIBER REINFORCED COMPOSITES

S. KYRIAKIDES, R. ARSECULERATNE, E. J. PERRY and K. M. LIECHTI

Engineering Mechanics Research Laboratory, Department of Aerospace Engineering and Engineering Mechanics, The University of Texas at Austin, Austin, TX 78712, U.S.A.

(*Received* 3 *November* 1993; *in revised form* 5 *July* 1994)

Abstract—In this paper a combination of experimentation and analysis is used to identify and study the mechanisms that govern the failure of unidirectional fiber composites under compression. The experimental part includes experiments in which the compressive strength and the prevalent failure mechanisms of AS4/PEEK composite are established, tests for establishing the constitutive properties of the composite and its constituents, and an evaluation of the extent of misalignment of fibers in manufactured composites. The failure load of the composite was confirmed to be affected by geometric imperfections in the form of fiber waviness, and failure was found to lead to kink bands with distinct orientations and widths.

Motivated by the experimental findings, the composite was idealized as a two-dimensional solid with alternating fiber and matrix layers, each having the measured properties of the two constituents. The compressive responses of microsections of finite width with imperfections of various spatial distributions were established numerically. The calculated responses are characterized by an initially stiff, stable regime terminated by a limit load instability which is associated with the strength of the composite. Following the limit load, the deformation localized into inclined bands with distinct widths. It has been verified that, as the localization process progresses, the fiber bending stresses at the ends of these bands grow to values comparable to those of the fiber strength. The sensitivity of the calculated response to the geometric characteristics of the imperfections was studied parametrically.

1. INTRODUCTION

Fiber reinforced polymer matrix composites offer higher stiffness and strength to weight ratios than monolithic structural materials. As a result, such composites have become attractive alternatives to aluminum in aerospace structures. More recently, these materials are being considered for submersible vehicles (Garala, 1987) and various offshore structures [see for example Salama (1986)] where the same advantages can lead to lighter and more effective structures. As is the case in many aerospace structures, in these new applications, the primary design loads are often compressive.

Early in their development it was observed that the compressive strength of such aligned composites was significantly less than their tensile strength (Dow and Gruntfest, 1960). In spite of significant improvements in other properties (e.g. impact resistance and tensile strength) the compressive strength of modern composites ranges between 50–60% of their tensile strength. This significantly reduces the advantageous position of these materials in structures in which compressive strength is the primary design requirement. As a result, the causes of this difference have attracted considerable attention over the last 30 years. The historical development of the problem in very broad terms is as follows. Rosen (1965), following the direction suggested by Dow and Gruntfest (1960), idealized fibers embedded in a matrix as elastic beams on an elastic foundation in order to estimate the compressive stress at which the fibers buckle. The lowest buckling stress is associated with a shear mode of buckling with long wavelengths and is given by

$$\sigma_C = \frac{G_m}{(1 - v_f)} \tag{1}$$

where G_m is the elastic shear modulus of the matrix and v_f is the fiber volume fraction of

the composite (using the rule of mixtures this reduces to $\sigma_C \approx G_{12}$, the shear modulus of the composite). He associated this critical buckling stress with the compressive strength of the material. The importance of shear in the onset of instability in aligned composites was also recognized by Hayashi (1965)† who obtained the same result from a somewhat different direction. Although some support for the appropriateness of this intuitively satisfying analysis came from experiments on idealized composites (see for example Greszczuk, 1975), it was clear from its inception that for commonly used fiber epoxy systems eqn (1) yields compressive strengths which are significantly higher than those measured. In spite of many extensions and improvements [see for example Sadowsky *et al.* (1967), Lanir and Fung (1972), Maewal (1981), Waas *et al.* (1990b), Lagoudas *et al.* (1991)] this remains the case today for all analyses in which the constituents are assumed to be elastic.

In the majority of the commonly used fiber composites, the compressive strains at failure are such that the matrix yields. The first effort to correct for this effect appears in Schuerch (1966) in his analysis of boron fiber–magnesium matrix composites. The essence of this effect, as clearly stated in Budiansky and Fleck (1993), is that eqn (1) is modified to

$$\sigma_C = \frac{\bar{G}_m}{(1-v_f)} \tag{2a}$$

where $\bar{G}_m$ is the so called *reduced shear modulus* of the matrix as predicted by the J_2 deformation theory of plasticity and can be expressed as

$$\bar{G}_m = \frac{G_m}{\left[1+3G_m\left(\frac{1}{E_{ms}}-\frac{1}{E_m}\right)\right]} \tag{2b}$$

where $(\cdot)_m$ refers to the elastic properties and $(\cdot)_{ms}$ refers to the secant modulus in the inelastic case [for details, see the review of plastic buckling by Hutchinson (1974)]. Instead of $\bar{G}_m$, Schuerch used the "tangent modulus of the equivalent stress–strain response" of the material modified for shear. His predicted failure stresses seem to be in reasonable agreement with three experimental points from a boron–magnesium composite that he tested [see also Lager and June (1969)]. However, eqn (2) in general yields predictions of failure stresses that are lower than those of eqn (1) but still significantly higher than measured results [see Budiansky and Fleck 1993)].

An important clue to the problem came from Argon (1972) who pointed out that fiber composites made by normal manufacturing techniques have regions of fiber misalignment. Compression leads to the development of local shear stresses in these regions. When these shear stresses reach the yield stress of the composite (σ_{12}^0), the shear modulus decays, and this results in local instability. He suggested that a more appropriate measure of the material strength is given by

$$\sigma_C = \frac{\sigma_{12}^0}{\theta_0} \tag{3}$$

where θ_0 is the local fiber misalignment angle, henceforth called fiber imperfection. He also pointed out that this mechanism is indeed still a shear mode of fiber buckling but that the local nature of imperfections, coupled with plasticity in shear, result in local buckling which develops into a kink band. The sensitivity of composite compressive strength to σ_{12}^0 was demonstrated by Piggott and Harris (1980) and by Piggott (1981) in experiments involving several fibers and matrices of varying properties.

Evidence has been growing that many aligned composites under compression fail by developing distinct bands of broken fibers which are at an angle of less than 90° to the direction of loading. Perhaps the most notable demonstration of this mode of failure came

† Pointed out by A. M. Waas.

from Weaver and Williams (1975) who compressed a relatively low fiber volume fraction carbon composite ($v_f \approx 0.36$) under varying values of hydrostatic pressure. Under these conditions, failure resulted in a local region of several kink bands which remained intact. In fact they reported residual strengths in their specimens on the order of 50–75% of the respective failure loads. Evans and Adler (1978) reported kink band failures in three-dimensional carbon–carbon composites. Under impact loading, fiber bundles aligned with the loading axis exhibited various forms of kinking. The support provided by the three-dimensional microstructure enabled them to capture the failure modes *in situ*. Waas *et al.* (1990a) used the stress concentration in the vicinity of a circular hole to initiate and capture kink band failures. Failure by kinking was also reported by Chaplin (1977), Piggott and Harris (1980), Parry and Wronski (1982), Hahn and Williams (1986), Hahn and Sohi (1986), Yurgartis and Sternstein (1988) and others.

Budiansky (1983) reaffirmed the sensitivity of the critical stress to imperfections and extended the analysis of Argon by considering the response of a zero angle kink band in an aligned composite with an elastic–plastic shear response. If the fibers are assumed to be inextensional, then this yields the following relationship between the applied axial stress and the induced shear strain (γ):

$$\sigma = \frac{\sigma_{12}(\gamma)}{(\theta_0 + \gamma)} \tag{4}$$

where $\sigma_{12}(\gamma)$ is simply the response of the composite to simple shear [the same result was also reported by Chatterjee and McLaughlin (1979) and by Schapery (1992) who considered a representative section of the composite with a uniform misalignment]. In the case where the shear response is elastic–perfectly plastic, the critical stress is obtained by replacing γ by its value at yield γ_0. A significant extension of this basic idea which includes analysis of inclined kink bands, combined axial and shear loading, and comparison with experimental values of σ_C is presented in Budiansky and Fleck (1993). [For a more detailed review of the subject see Camponeschi (1991).]

In the present work we accept the premise of Argon's arguments and, through a combination of experiment and analysis, try to illustrate how actual imperfections influence the response and failure of composites to compression. We will demonstrate that failure is initiated by a limit load instability, as implied by eqn (4), which is followed by localization of deformation which results in kinking.

2. EXPERIMENTS

All experiments were conducted on ICI APC-2/AS4 composite with a fiber volume fraction (v_f) of 0.60 [APC-2 is a PEEK (poly-ether-ether-ketone) thermoplastic matrix and AS4 is a PAN-based Hercules fiber]. Flat coupon-type and cylindrical solid rod specimens were cut from a $12 \times 24 \times 0.75$ in ($305 \times 610 \times 19$ mm) plate which was hand laid using 12 in (305 mm) wide prepreg. Ring and tubular specimens were machined from thin-walled, filament wound tubes made from 0.25 in (0.635 mm) tape of the same material. Four different sets of experiments were conducted with the following objectives:

(i) establish dependable values of the compressive strength of the material;
(ii) provide basic information on the causes and results of failure;
(iii) provide a quantitative assessment of the imperfections present in the material used;
(iv) establish a complete set of mechanical properties first of the composite and secondly of its constituents, in order to facilitate the analytical phase of the work.

A summary of the experimental procedures and of the results of each of the first three efforts are presented below. Material characterization experiments and results are briefly outlined in the Appendix. The measured properties are listed in Table 1.

Table 1. Material properties measured

(a) APC-2/AS4 Composite

E_{11} msi (GPa)	E_{22} msi (GPa)	G_{12} msi (GPa)	ν_{12}	v_f
18.62 (128)	1.533 (10.57)	0.84 (5.79)	0.3	60%

(b) AS4 Fibers

E_f msi (GPa)	$\hat{\sigma}_f$ ksi (MPa)	n_f	ν_f
31.0 (214)	600 (4.14)	1.9	0.263

(c)APC-2 Matrix

E_m msi (GPa)	σ_{mo} ksi (MPa)	ν_m
0.89 (6.14)	11.9 (82.1)	0.356

2.1. *Compressive strength experiments*

Compression tests are inherently difficult and require consideration of specimen stability and load alignment as well as high stiffness testing facilities. These difficulties are accentuated in the case of aligned composites which have high axial strength and stiffness but have poor transverse properties. The response to axial compression and strength of the composite studied was established through two types of experiments which were selected because they maximize load uniformity in the test section and specimen alignment and also minimize end effects.

The first method involved testing of 0.375 in (9.525 mm) diameter cylindrical rod specimens ground from square blocks cut from the plate mentioned before. The test sections were 1.0 in (25 mm) long and 0.325 in (8.255 mm) in diameter. The specimen's overall length was 3 in (76 mm). Steel cylindrical end supports with honed bores were snugly fitted to the ends of the specimens as shown in Fig. 1. The assembly slides inside a thick aligning sleeve

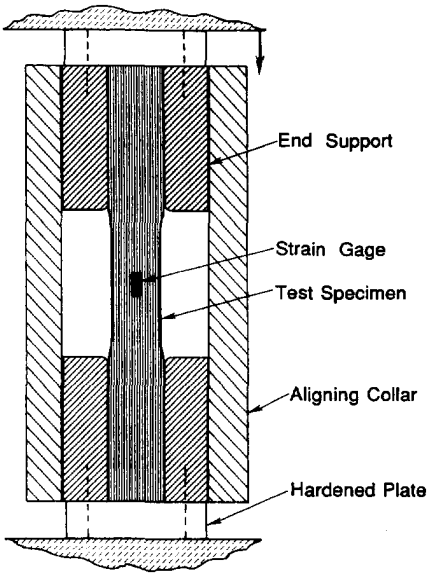

Fig. 1. Compression test fixture for unidirectional, circular rod composite specimens.

Table 2. Measured compressive strengths and corresponding strains

(a) Rod experiments

Number	σ_C ksi (GPa)	ε_C (%)
1	163.1 (1.125)	1.041
2	163.7 (1.129)	1.026
3	151.4 (1.044)	0.948
4	165.1 (1.139)	1.018
5	167.7 (1.156)	1.040

(b) Confined ring experiments

Number	σ_C ksi† (GPa)	ε_C (%)
1	142.4 (0.982)	0.859
2	157.0 (1.082)	0.968
3	175.5 (1.210)	1.088
4	131.0 (0.903)	0.779
5	174.2 (1.201)	1.080
6	148.4 (1.024)	0.907
7	167.8 (1.157)	1.040
8	140.1 (0.966)	0.843
9	158.4 (1.093)	0.978
10	152.6 (1.053)	0.939
11	155.2 (1.070)	0.956

† Calculated values

as shown in the figure. All sliding surfaces were ground and honed to close tolerances. The axial load was applied through hardened and ground end plates which were in contact with parallel rigid bearing plates connected to a universal testing machine. Loading was applied under displacement control and resulted in a strain rate of 0.0067% per second. Small strain gages bonded to the specimen test section were used to measure the axial strain.

Five experiments of this type were carried out. In all cases failure was sudden and catastrophic and resulted in the breaking of the specimen into two sections. All failures occurred in the specimen test section. The maximum stress and strain recorded in each case are listed in Table 2(a) and plotted in Fig. 2.

A second set of compression experiments involved hoop wound thin-walled rings tested in the confined arrangement shown in Fig. 3 [similar to that proposed in Tarnopol'skii and Kincis (1985); also used by Kim and Tsai (1988)]. The composite ring is stabilized by a thick, contacting compliant ring. The two ring assembly is inserted into a stiff retainer as shown in the figure. The compliant ring is axially compressed through a stiff loading ring. The radial deformation of the polymeric ring causes circumferential compression of the test specimen. The circumferential strain in the specimen was monitored by three strain gages bonded on the inner surface of the specimen. The specimens were ground finished to an outer diameter of 3.820 in (97.3 mm) and wall thickness of 0.026 in (0.66 mm). The

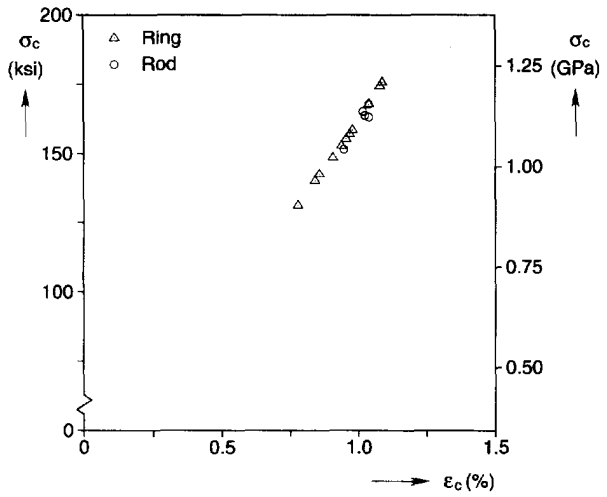

Fig. 2. Critical strains and stresses from experiments on APC-2/AS4 rod and confined ring specimens.

geometry and material properties of the compliant ring strongly affect the performance of this testing scheme. In our case, a 0.62 in (15.7 mm) thick, high density polyethylene ring was found to provide the radial support required to avoid buckling and a compliance that kept the load requirements within the 50 kip (220 kN) range of our testing machine. More details about the design and operation of this testing device can be found in Arseculeratne (1993).

This testing scheme has the advantage of being free of end effects which play a spoiler role in many standard compression testing methods used in composites [see a critical review in Arseculeratne (1993)]. The arrangement used in this study was found to result in uniform deformation in the specimen up to failure. A disadvantage is that the stress in the specimen is not easily measured with accuracy and will not be quoted for this set of results.

Eleven composite rings were tested to failure using this test method. In all cases the failure was sudden and catastrophic and took the form of one sharp break, as shown in Fig. 4, which was at a small angle to the axis of the ring. This angle varied from specimen to specimen and was in the range of 0° to 15°. The failure strains achieved are listed in Table 2(b) and also appear in Fig. 2 (the failure stress was evaluated from the compressive stress–strain response of the material using the measured failure strains). Comparing the two sets of failure strains, it is interesting to observe that the highest values recorded came from the ring specimens. At the same time, the ring results exhibit significantly larger scatter than the rod results. It is the premise of this paper that fiber imperfections play a decisive factor in the failure of the material. It was observed that the innermost layers of the filament wound rings had larger imperfections than bulk material. We believe this to be the cause of the larger scatter in the ring results.

Overall, the higher values of failure stresses and strains in Tables 2(a) and (b) are among the highest reported to date for this material [Kim and Crasto (1992) reported strengths from composite–matrix sandwich test specimens which are 28% higher].

2.2. *Failure modes*

2.2.1. *Confined rod experiments.* As reported above, the failure of aligned composites under compression is sudden and catastrophic. As a result, the evaluation of the mechanisms that are responsible for failure from fractographic analyses is difficult. We observed that the most effective reports of kinking in fiber composites came from experiments in which the failure region was confined either by the composite itself (Evans and Adler, 1978) or by the loading scheme used (Weaver and Williams, 1975; Waas *et al.*, 1990a). Indeed, confinement of the test specimen is a standard practice in the testing of other materials with a high degree of anisotropy such as rocks, where kinking is the prevalent mode of failure [see for example Paterson and Weiss (1966)].

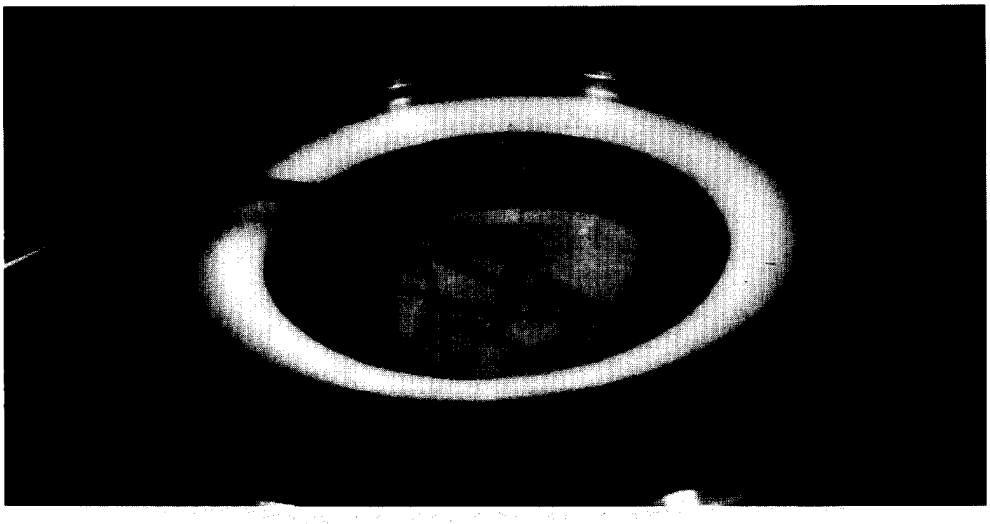

(a)

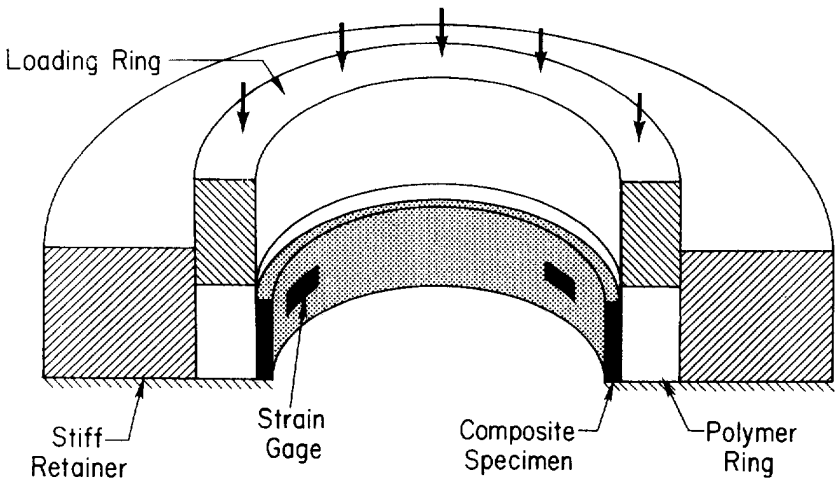

(b)

Fig. 3. Confined ring tester: (a) photograph of device; (b) schematic of device and components.

Fig. 4. Photograph of a failed ring tested in the confined ring tester.

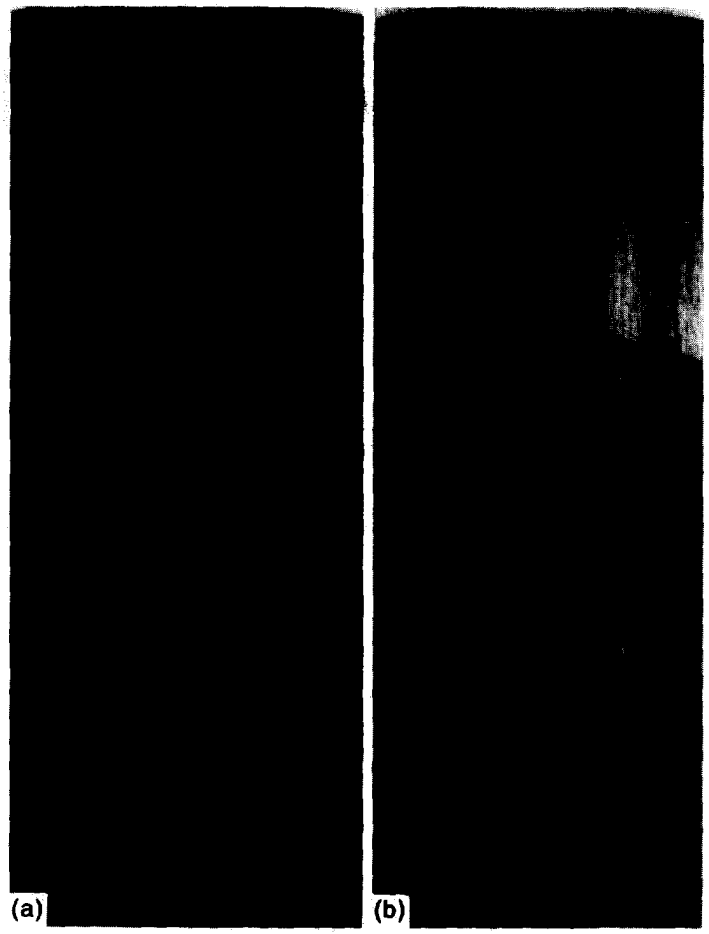

Fig. 7. Pictures of specimens with failure zones preserved due to confinement: (a) specimen with multiple kink planes. Several were formed at the initiation of failure and others subsequently at the propagation stress level; (b) specimen with four kink planes formed at the initiation of failure.

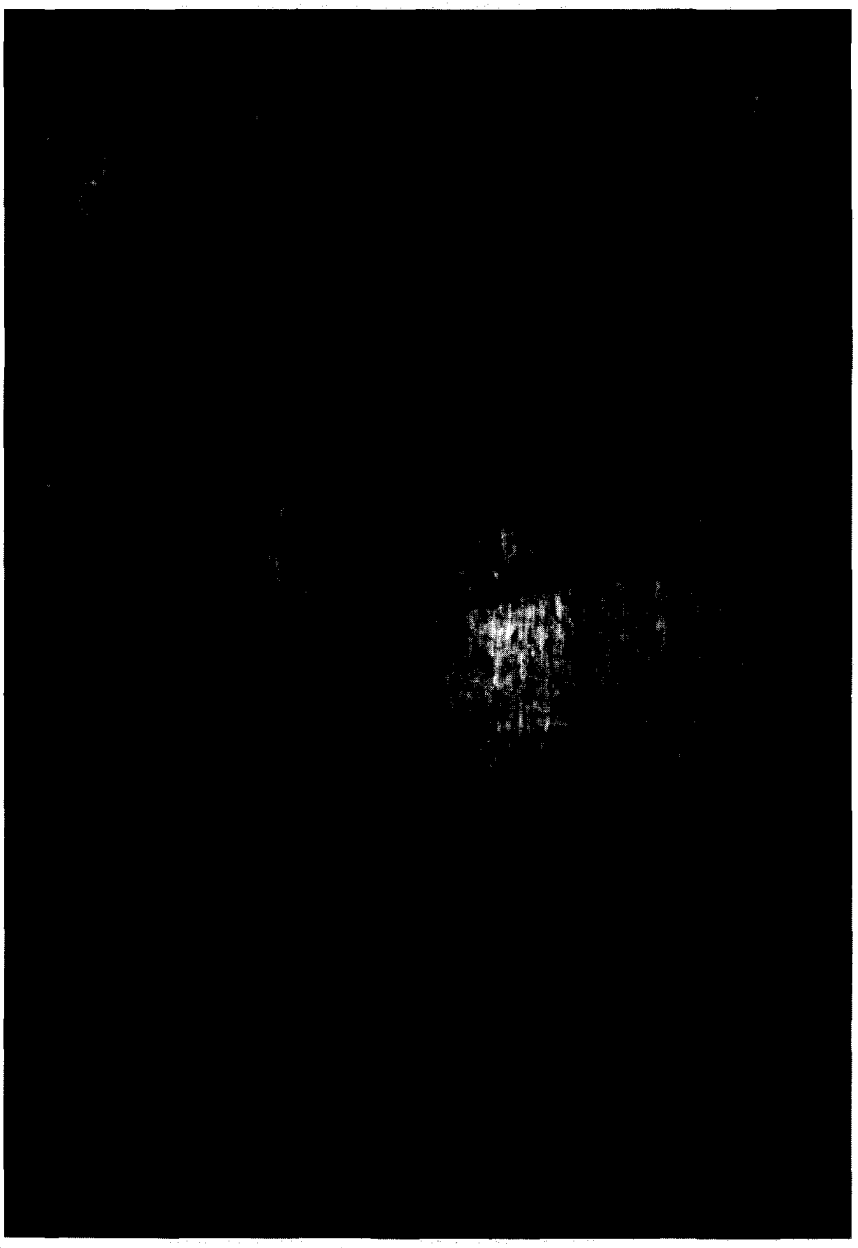

Fig. 8. A higher magnification view of the specimen in Fig. 7(a) [rod diameter = 0.375 in (9.53 mm)].

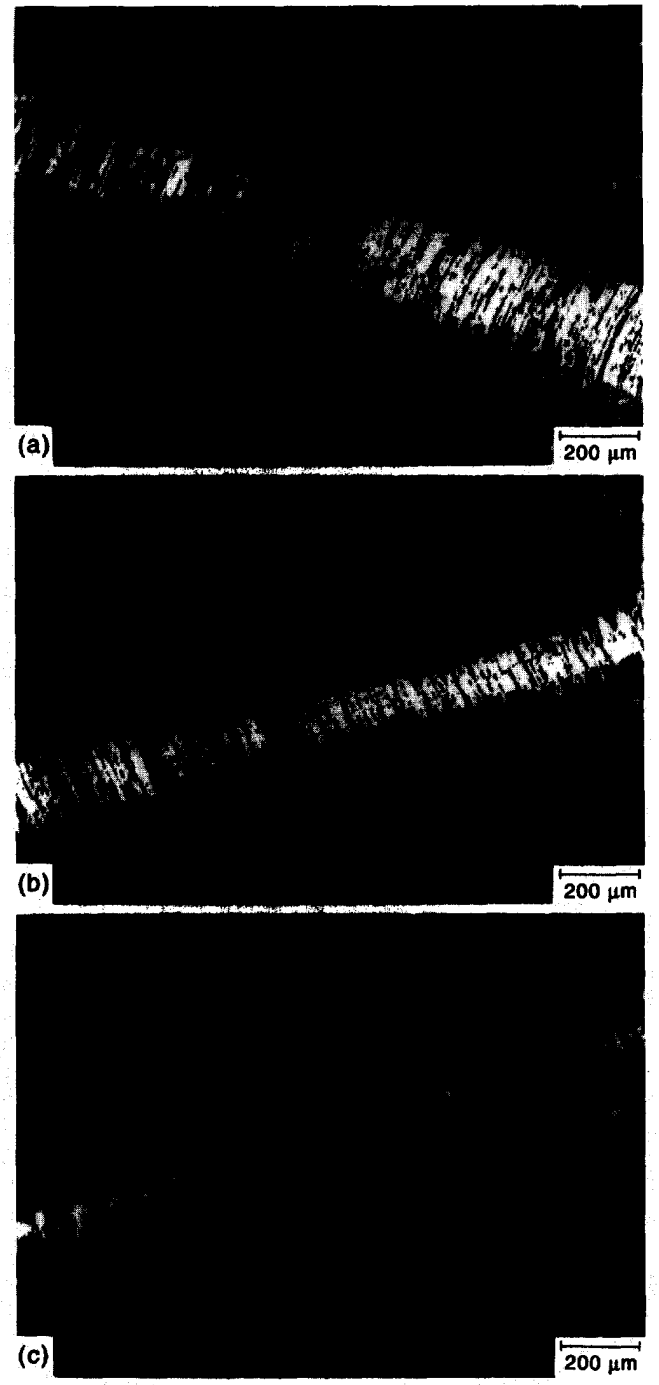

Fig. 9. Photomicrographs of three kink bands on the surface of a specimen.

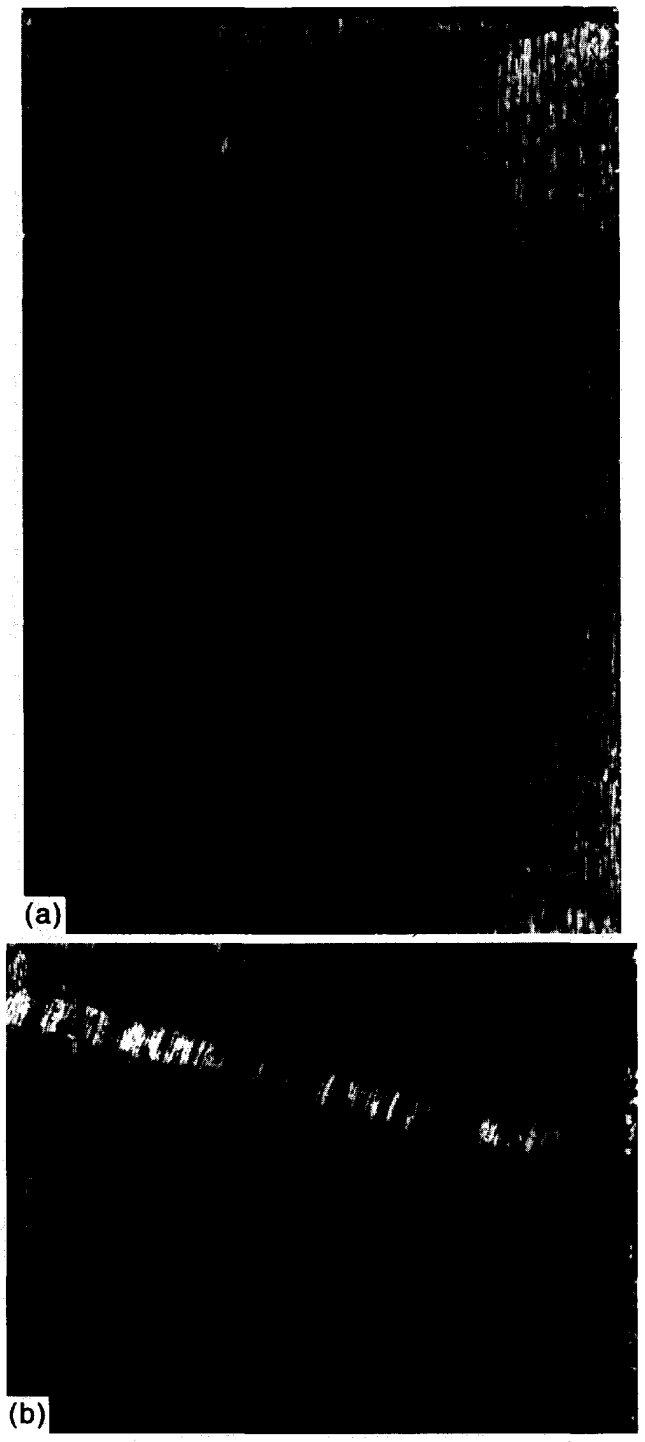

Fig. 10. Kink bands on a plane passing approximately through the axis of the rod obtained by grinding a failed specimen: (a) global view; (b) high magnification view.

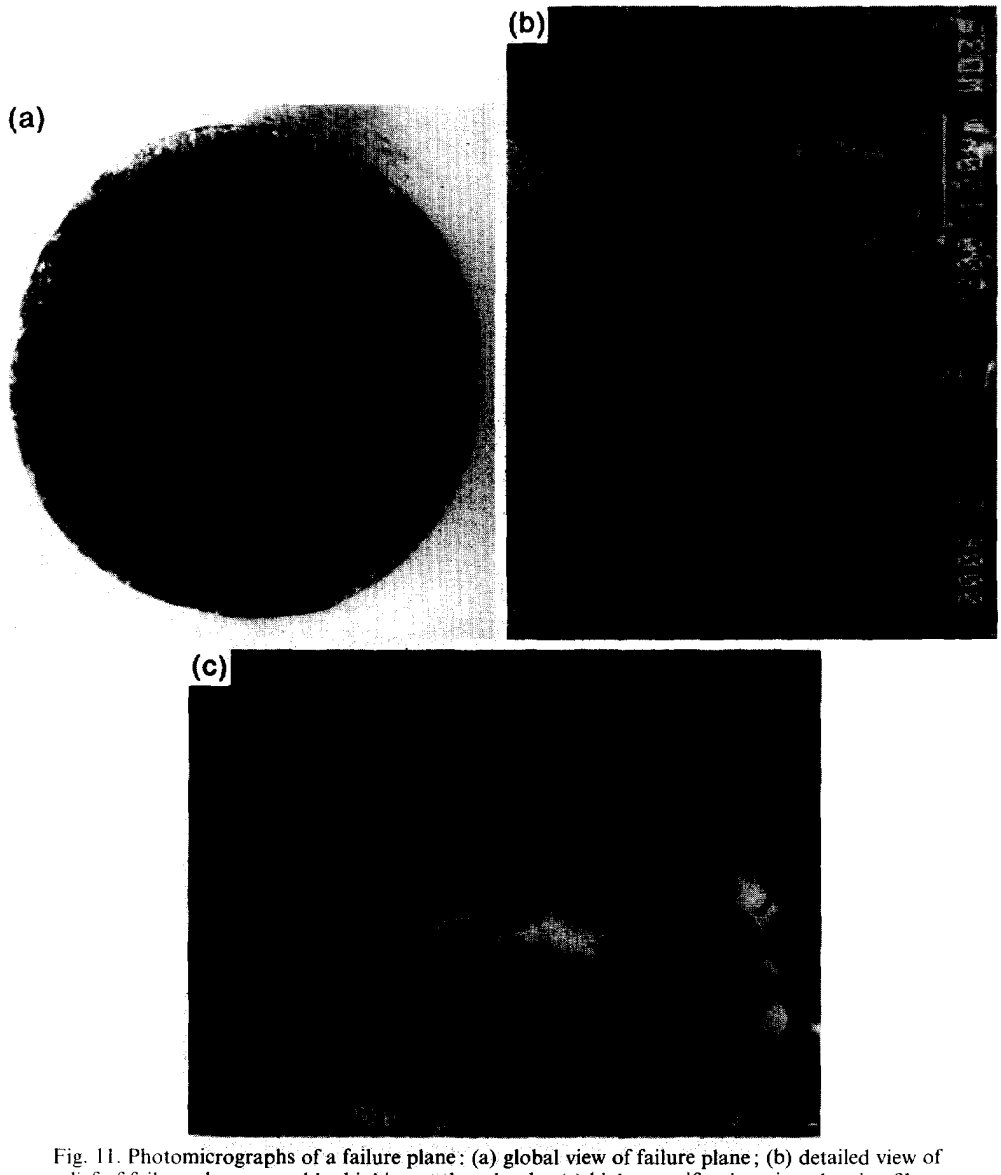

Fig. 11. Photomicrographs of a failure plane: (a) global view of failure plane; (b) detailed view of relief of failure plane caused by kinking at three levels; (c) high magnification view showing fibers which have failed by bending (fiber diameter = 7 μm).

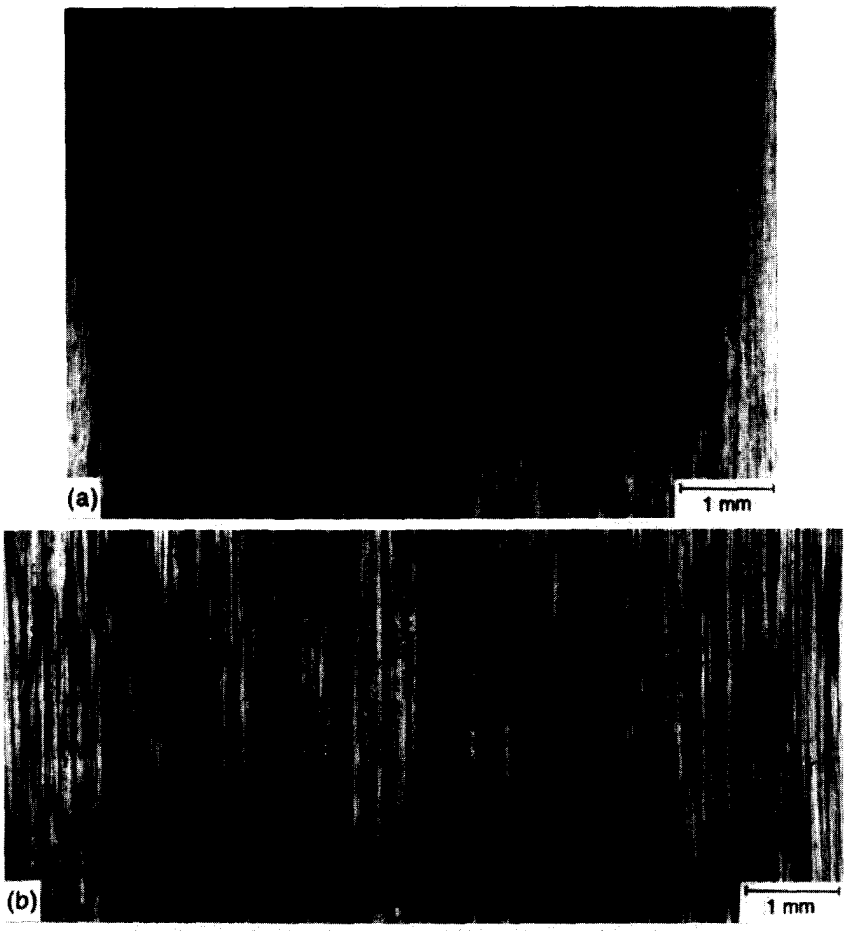

Fig. 12(a). Photomicrograph of APC-2/AS4 prepreg showing bands of misaligned fibers; (b) photomicrograph of composite after curing showing similar bands of misaligned fibers.

Fig. 13. A higher magnification view of a band of misaligned fibers in the composite tested.

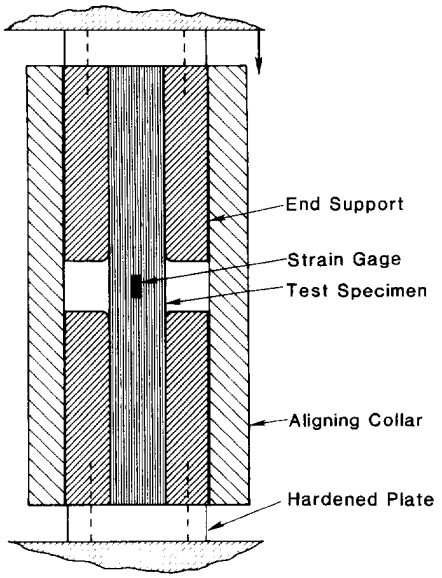

Fig. 5. Compression test fixture used to test composite rods with confined ends.

From preliminary experiments we confirmed that confinement was a method of limiting the extent of post-failure deformation. The experimental arrangement that was used to test solid rod specimens was modified somewhat in order to cause failure to occur in a confined region of the specimen. The modified arrangement is shown in Fig. 5. It differs from that shown in Fig. 1 in two ways. The test specimen cross section is uniform [0.375 in (9.53 mm) diameter] and the cylindrical end supports are now 1.25 in (31.8 mm) long. Under these circumstances a small stress concentration (estimated to be of the order of 1.1–1.2) develops near the outer radius of the specimen at the interface with the corner of the hardened plate. As a result, failure initiated at one of the confined ends. Under displacement controlled loading, the extent of failure could be limited.

A typical axial stress versus end-shortening response obtained from such an experiment is shown in Fig. 6. The pre-failure response is essentially the same as that from the more conventional specimens reported in Section 2.1. Failure was again sudden and occurred at a stress level which was generally somewhat lower than those in Table 2(a) [158 ksi (1.09

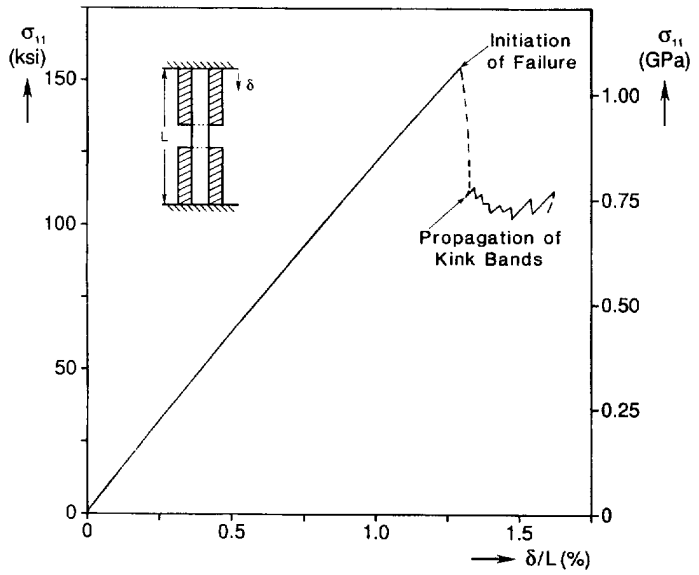

Fig. 6. Axial stress end shortening response recorded in a confined rod experiment.

GPa) for the case shown]. In the process, the load dropped by approximately 30% in a dynamic (uncontrolled) way. The failure is local in nature and took the form of kinking which is confined to planes (approximately) that are at an acute angle to the 2-axis of the material. Figure 7(a) shows the surface of a specimen failed in this fashion. Failure initiated at one end of the test specimen and was arrested due to the radial confinement. Confinement limits the extent to which the kink bands can deform and, as a result, the energy that can be dissipated. Initially, the loaded specimen has sufficient energy for the formation of more than one kink plane each of which is initiated from the weakened region formed at the termination of the previous kink plane. In this experiment, compression was continued past first failure and resulted in the jagged load plateau seen in Fig. 6. Each load peak on the plateau corresponds with the initiation of one or two additional kink planes. A total of 14 kink planes were formed before loading was terminated [12 of the kink planes can be seen in Fig. 7(a)]. All kink planes are oriented in such a way so that their normals are approximately co-planar.

Additional experiments were conducted in which the failure mechanism outlined above was found to be repeatable. In order to better understand the sequence in which the events described above take place, several experiments were terminated after the first drop in load was recorded. A test specimen from such an experiment, shown in Fig. 7(b), can be seen to have developed only four kink planes. A total of five such experiments were conducted and the number of kink planes formed during this initiation stage of failure was found to vary from three to seven.

In order to assess the effect of confining pressure on failure, in several experiments the diameter of the rods was varied by a small amount [within 7×10^{-4} in (18 μm); some rods had to be press fit into the end sleeves] thus varying the initial contact pressure provided by the end sleeves. This did not affect either the stress at initiation of failure (σ_C) or the stress plateau (σ_P) at which the number of kink planes form in a noticeable way. The variation in these critical stresses in the experiments conducted was as follows:

σ_C† ksi (GPa)	σ_P‡ ksi (GPa)
138–158 (0.952–1.09)	112–119 (0.772–0.821)

† 10 experiments ‡ 5 experiments.

One observable effect that the confinement had on failure was that as the confining pressure increased, the deformation in the kink planes (rotation of broken fibers) was reduced.

From these experiments we conclude that once failure is initiated inside the confined configuration described, more kink planes can be developed at a well defined stress level which is lower than that which was required to initiate failure. This type of behavior is reminiscent of other *propagating instabilities* known to affect several materials and structures [see Kyriakides (1993)]. This class of instabilities are characterized by three phases. The first is the initiation phase where the structure becomes unstable for the first time. This global instability is usually associated with a load maximum (limit load). The limit load is usually followed by localization of deformation which is the second characteristic phase. Localized deformation is then arrested due to reasons that are unique to each of the problems exhibiting this behavior. Finally the instability starts spreading (propagating) into the intact domain of the structure. The lowest load at which the instability will spread corresponds to steady-state quasi-static propagation and is given the name of *propagation load*. In many of the known examples of this behavior, the propagation load is significantly lower than the load required to initiate instability in the intact structure.

Clearly, the present problem has the three phases described above. In the theoretical section of this work we will demonstrate that the material exhibits a limit load instability [this is in fact also implied by eqn (4)] which is very imperfection sensitive. We will also demonstrate that kinking is the final stage of localization. In our confined rod experiments, kinking in a particular plane is arrested when it reaches the wall of the confinement. The

weakened region around the intersection of the previous kink plane with the confining wall acts as the initiator for the formation of the next kink plane.

In other problems exhibiting propagating instabilities, the propagation load is a characteristic load of the solid or structure. In the present problem, it is not yet clear whether σ_P, as defined, is a characteristic stress of just the finite, confined configuration we used or if it is representative of the stress of propagation of kink planes in bulk material.

2.2.2. *Kink planes and kink bands.* Kink planes and kink bands from the confined rod experiments were studied in detail using optical and scanning electron microscopes. Two sets of observations and measurements were made. The first involved kink bands on the cylindrical surface of specimens and the second involved kink bands in the interior of a specimen. Figure 8 shows a higher magnification view of several of the kink planes on the surface of the specimen shown earlier in Fig. 7(a). The intersection of the kink planes with the cylindrical surface of the specimen is not straight indicating that, rather than being planes, the kinked regions are somewhat curved, at least at their outer edges. We also observe that fiber rotations in adjacent kink planes are in opposite directions for maximum compatibility with the confinement.

Micrographs of three kink bands from the surface of this specimen are shown in Fig. 9. As reported by others, the kink bands are bands of broken fibers. The kink bands were found to be oriented at angles of 12° to 16° to the 2-axis of the material. The widths of these kink bands were found to vary from 0.003 to 0.010 in (76 to 255 μm) or approximately from 11 to 36 fiber diameters (AS4 fibers typically have diameters of 7 μm). These ranges of kink plane angles and kink band widths were repeatable in all experiments conducted.

A view of the kink planes inside another specimen is shown in Fig. 10(a). In this case, a failed specimen was potted in a steel/epoxy potting compound and approximately half of it was removed by surface grinding along the axis of the rod. As remarked upon earlier, the kink planes are oriented in such a way that their normals are co-planar. This claim is supported by the view shown in Fig. 10(a) which comes from a plane very close to the one formed by the normals to the kink planes. Most of the intersections of adjacent kink planes are seen to have congruent angles and to occur at the widest point of the specimen. We also observe that in this plane the kink bands are quite straight and their widths vary less than those on the surface of the specimen. The kink band angles vary between 12° and 16.5°, that is, they are approximately the same at the angles measured in kink bands on the surface of the specimen. The kink band widths vary between 0.0058 and 0.0087 in (150–220 μm) or approximately between 20 and 30 fiber diameters. At the top of the specimen we observe the intersection of the cut plane with a concave kinked surface which spans the width of the specimen. We suspect that this was the location where failure initiated.

Several intersections of kink planes can be seen in Fig. 10(a). An expanded view of one of the intersections is shown in Fig. 10(b). The opposite orientations of the kinked fibers in adjacent kink planes is clearly visible. The detail of the corner of intersection of the two planes supports the premise that the termination of a kink plane provides the imperfection for the initiation of the next kink plane.

Another failed specimen was separated into two pieces, along one of the kink planes, by lightly tapping on the intact end of the test specimen. Figure 11 shows three views of increasing magnification of this plane. In Fig. 11(a) we observe that the failure surface has distinct relief which resulted, at least in part, from separating the failed specimen into two sections. The nature of this relief is clarified in Fig. 11(b) where kinking is seen to have taken place on at least two different levels. Figure 11(c) shows a much higher magnification micrograph which gives us details about the nature of failure at the fiber level. The fibers failed by bending and, at least in this neighborhood, the direction of bending is uniform [similar bending failures have been reported in Ewins and Potter (1980)].

2.3. *Fiber imperfections*

Although it is well known that fiber imperfections play an important role in the failure of aligned composites, quantitative information on such imperfections is very limited

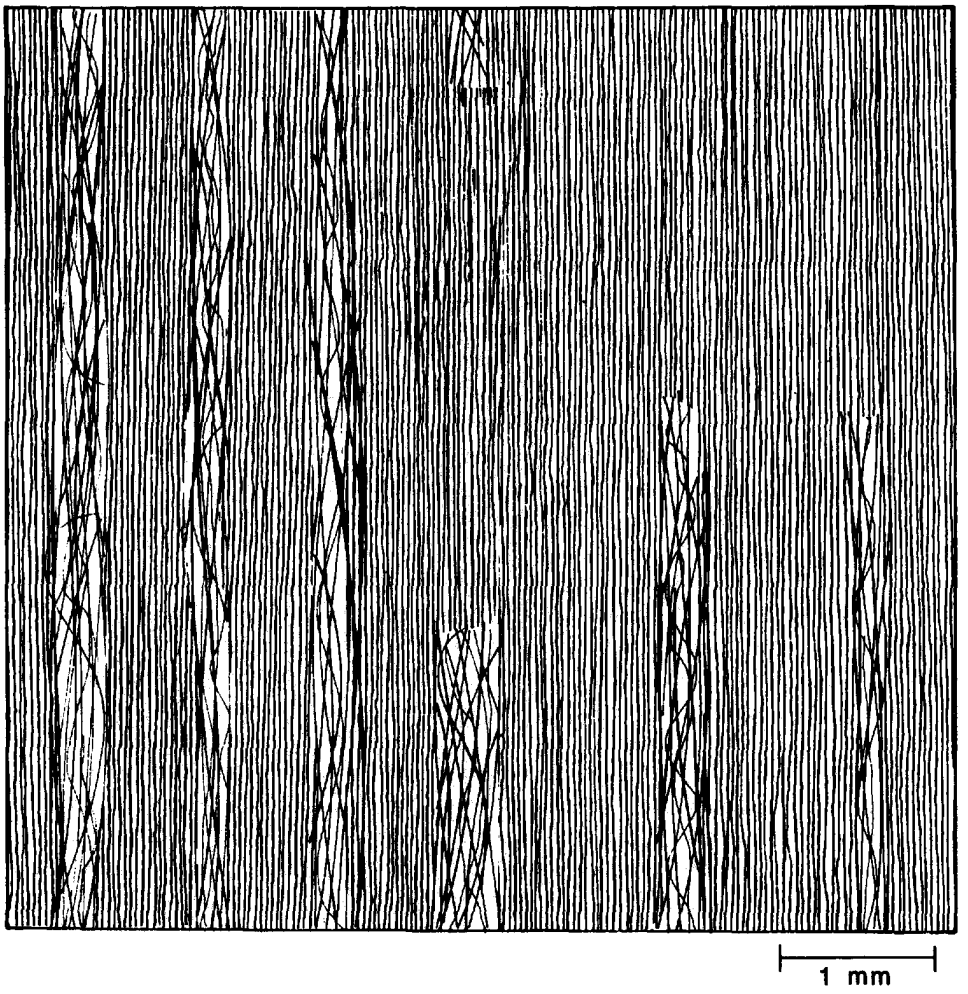

Fig. 14. Sketch of distribution of fiber imperfections in a representative composite section.

[Yurgartis (1987) made local measurements of fiber misalignment]. Imperfections are introduced during the manufacturing of the material (e.g. the prepreg) and of the structure. Prepreg manufacturing methods are often proprietary and vary from one manufacturer to another. The manufacturing of composite structures is even more varied, and in each process fiber imperfections depend on a number of variables. Information on the effect of each variable on compressive strength is non-existent. Indeed, in view of its importance, this area seems to be in need of a more serious examination.

A limited effort to quantify imperfections present in the material used in this study was undertaken. Our bulk composite was a 0.75 in (19 mm) plate assembled by hand laying 0.005 in (0.125 mm) prepreg. Sections at different depths through the plate were examined under a microscope in order to understand the nature of fiber imperfections. A low magnification view of approximately what was observed at all depths appears in Fig. 12(b). Although some fiber misalignment exists throughout the material, imperfections are more severe in bands which are periodically distributed along the 2-axis of the composite. A close-up view of one of these imperfection bands is shown in Fig. 13. This particular one is approximately 0.04 in (1 mm) wide and the increased waviness of the fibers within it is quite obvious. At the same time, the density of the fibers inside the band is smaller than that of the neighboring material.

The spatial distribution of imperfection bands in a somewhat larger section [0.24 in (6 mm) square] of the material is shown schematically in Fig. 14. The bands are rather regularly spaced, and several continue over the whole height of the region shown whereas some terminate in this region. The distance between the bands varied between 0.040 and

0.060 in (1.0–1.5 mm), and band widths of up to 0.15 in (3.8 mm) were measured. The fiber waviness inside the bands was three-dimensional in nature (in plane and out of plane).

The rather regular distribution of the bands suggested that they may be the result of the manufacturing of the material rather than the plate. Indeed, this was confirmed by conducting a similar examination of the prepreg used to construct the plate. A micrograph of the prepreg is shown in Fig. 12(a). Similar types of imperfection bands as those seen in the plate can clearly be observed here (note that this is a thermoplastic and, as a result, the prepreg is in a cured condition). In some cases the bands are so well formed that light passes through them.

The process used to manufacture this prepreg is proprietary. In broad terms, however, a 12 in prepreg is made by feeding 54 0.25 in fiber bundles wetted with matrix through an aligning and pressing machine. Each of the bundles is made up of four 3000 fiber tows. This implies first, that some overlapping of fiber tows takes place, and second, that the nominal spacing between the tows is 0.055 in (1.4 mm). In view of the closeness of this distance to those we measured, and lacking additional information, we speculate that the imperfection bands seen in the prepreg may have originated from the interfaces of the bundles and of those of the constituent tows. Whatever the cause of uneven distribution of fibers in these bands, subsequently, during manufacturing of a laminate, they become bands of higher resin content. During cool down, the alignment of fibers in these bands may even get worse resulting in the types of imperfections shown in Fig. 13. The distribution of these bands varies sufficiently across one prepreg that it is reasonable to expect that the distribution of the bands through the thickness of the plate will vary from lamina to lamina, that is every five thousands of an inch. However, we reiterate the fact that the waviness within each band is three-dimensional.

Although these observations come mainly from the particular prepreg used to manufacture the composite specimens of this experimental program, we point out that similar imperfections have been observed in at least one more commonly used thermoplastic prepreg. The importance of such imperfections to the compressive strength of the composite is high. In view of this, the subject requires a more careful investigation.

The nature of fiber waviness inside several of the imperfection bands were examined in some detail. The imperfections measured were found to have half wavelengths (λ) and amplitudes (a) in the following ranges [normalized by the fiber diameter which is taken to have the nominal value of 7 μm (0.28×10^{-3} in)]:

λ/h	a/h
150–400	3–10

No further correlation between the measured amplitudes and wavelengths was observed. Fiber imperfections outside the bands were in general much smaller in amplitude than the ones quoted above.

3. ANALYSIS

It is instructive to first consider the compressive strengths of our specific composite which are predicted by various bifurcation calculations, that is, by analyses in which the fibers are assumed to be perfectly aligned and failure is associated with the stress at which the first alternate equilibrium becomes possible. We will quote results from the elastic fiber–elastic matrix analysis of Rosen (1965) [i.e. eqn (1)] and from its improved version given in eqn (2) in which the plasticity of the matrix is taken into account. A more general stability analysis of the same problem in which composites with alternating layers of two isotropic, nonlinear, finitely deformed solids are compressed under plane strain conditions was developed by Triantafyllidis and Maker (1985) and extended in Geymonat *et al.* (1993). This analysis was used (Triantafyllidis, 1993) to establish critical stresses for our composite using the measured nonlinear properties of both constituents presented in the Appendix

(both materials were idealized as J_2 deformation theory solids). The critical strains predicted by each of these three analyses are as follows:

Analysis	$\varepsilon_C(\%)$
Rosen (1965) equation (1)	4.4
Equation (2)	3.37
Triantafyllidis (1993)	2.9

The predicted failure strains are seen to be uniformly higher than those measured in our experiments (see Table 2). In spite of its refinements, the last of the three analyses quoted above yields bifurcation strains which are almost three times those measured. This difference reinforces Argon's argument (1972) that fiber imperfections play a decisive role in the compressive strength of such composites. Influenced by this, we use the insight developed in the experimental phase of this study to model and simulate the onset and progression of failure in imperfect composites using representative microsections of the material. Although it is realized that inertial effects do influence the progression of at least the type of failure observed in our experiments, they will be neglected in this first attempt at the problem.

The composite is idealized as a two-dimensional periodic array of imperfect fibers and matrix as shown in Fig. 15. (This is partly motivated by the experimental observation that the normals of all kink planes in the rod specimens were co-planar.) Fibers are assumed to be of uniform thickness h. The matrix layers have the width necessary for v_m to have the required value (0.40 for most calculations). Waas *et al.* (1990b) and Babich and Guz (1992) demonstrated that free boundaries lower the bifurcation load of such composites. In view of this, the composite microsections analysed were of finite width b, which will be defined by the number of fibers n_f.

The properties of each constituent are those measured in the experiments described in the Appendix, that is, the properties of AS4 fibers and PEEK (APC-2) matrix. The matrix is modeled as an elastic–plastic isotropic solid which undergoes finite deformations (finite deformation, J_2 flow theory of plasticity). The stress–strain response used is that in Fig. A4

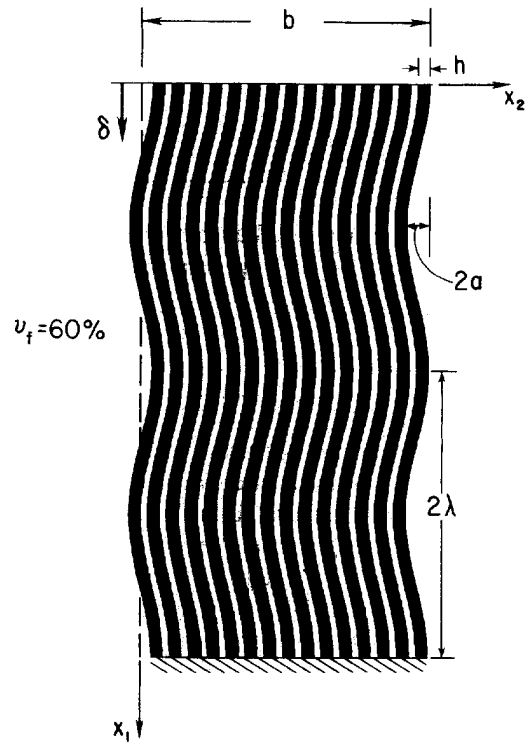

Fig. 15. Geometry of idealized composite microsection with sinusoidal imperfections.

with the assumption that the material is perfectly plastic beyond a strain of 8%. Any rate dependence of this response is neglected at this stage. Although it is well known that carbon fibers are anisotropic [see Johnson (1987)], relatively little is known about their transverse properties. In this study they were idealized either as linear or as nonlinear, isotropic solids with an axial stress–strain response corresponding to that obtained from compression (Fig. A6). The nonlinearity was modeled through the J_2 deformation theory of plasticity using the data provided in Table 1(b). In cases where the fibers were assumed to be linearly elastic, the elastic modulus and Poisson's ratio given in Table 1(b) were used. The domain of each problem is discretized with finite elements using the computer program ABAQUS† with eight node biquadratic elements.

The main thrust of the analysis is to use the experimental observations about the nature and magnitude of fiber imperfections in our composite to investigate their effect on the onset and progression of compressive failure. Fiber imperfections will be sinusoidal, but microsegments with several different spatial imperfection distributions will be considered.

3.1. *Uniform sinusoidal imperfections*

The first case analysed involves a microsection of width b which has uniform sinusoidal imperfections of the type shown in Fig. 15. The imperfections are represented by

$$v_0 = a\cos\frac{\pi x_1}{\lambda} \tag{5}$$

where a is the amplitude and 2λ their wavelength. Because of symmetry, it is sufficient to consider a microsection of length (L) of only one quarter of the imperfection wavelength. We will discuss the major features of the calculated response of such a composite microsection through an example in which the fibers are assumed to be linearly elastic, $\lambda = 150h$, $a = 2h$, and $n_f = 60$. The calculated average axial stress (σ_{11})–end shortening (δ) response is shown in Fig. 16(a). The initial and five deformed configurations of the microsection are shown in Fig. 17 (for better interpretation of the deformation fields, the microsections shown are half a wavelength long). The configurations are numbered so as to correspond to the points identified by numbers in circles on the σ_{11}–δ response.

The response in Fig. 16(a) initially is relatively stiff and almost linear. It becomes progressively nonlinear and, at a stress of approximately 151 ksi (1.04 GPa) and a strain of 0.79%, a load maximum is reached (point ②). This progressive reduction in the stiffness of the specimen is partly due to the geometric nonlinearity resulting from the imperfection combined with the nonlinearity of the matrix. In the central part of the microsection, where the fibers had the largest initial misalignment, in addition to axial stress the matrix is required to support increasingly higher shear stresses. As the two stresses increase, the modulus of the matrix decreases (see Fig. A4). As a result of these nonlinearities, the overall stiffness of the composite is progressively reduced, and a limit load eventually develops. In this case, at the limit load, the equivalent stress in the matrix reached a maximum value (in the central part of the specimen) of approximately 20.5 ksi (141 MPa), and its shear modulus was reduced by approximately 90%. The maximum compressive and tensile stresses in the fibers are plotted in Figs. 16(b) and (c) respectively. At the limit load (point ②) they are seen to be compressive throughout the specimen and, away from the ends, are approximately 260 ksi (1.79 GPa). At the two free edges, modest stress concentrations are observed which decay within a boundary layer of a few fibers (on the order of five).

Beyond the limit load, the axial stress is seen to decrease and, at the same time, the net contraction (δ) of the microsection also decreases (Riks' method, as modified in ABAQUS, is used to trace this part of the response). σ_{11} and δ continue to decrease simultaneously up to approximately point ⑥ on the response when δ starts to increase again while the average stress that can be carried continues to drop. The cause of this behavior becomes evident from the microsection deformed configurations. Following the limit load, the deformation localizes to a band which can be seen in configurations ③–⑨ in Fig. 17 to have distinct

† We are grateful to Hibbitt, Karlsson and Sorenson, Inc. for making ABAQUS available under academic license.

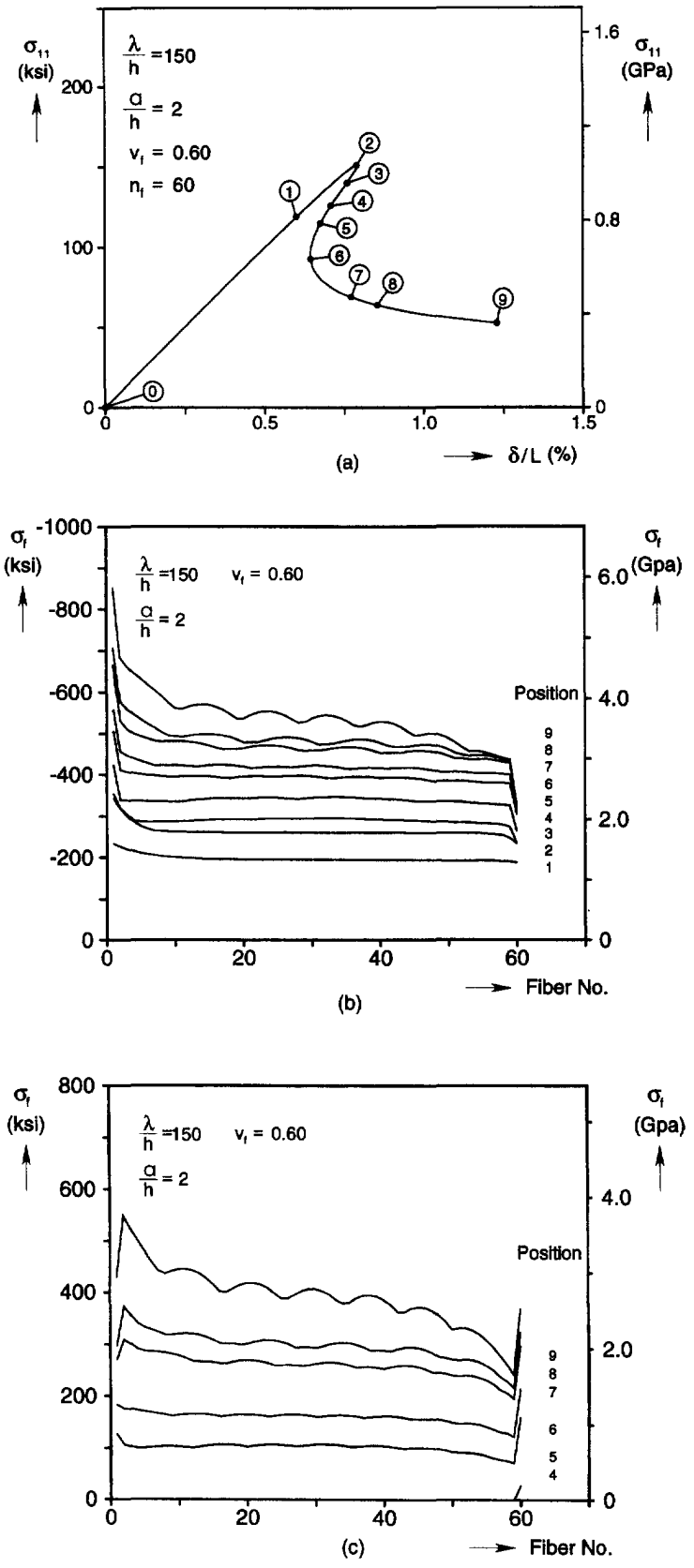

Fig. 16. Analysis of a microsection with uniformly distributed imperfections: (a) axial stress–end shortening response; (b) maximum compressive stresses in fibers at several points on response; (c) maximum tensile stresses in fibers at several points on response.

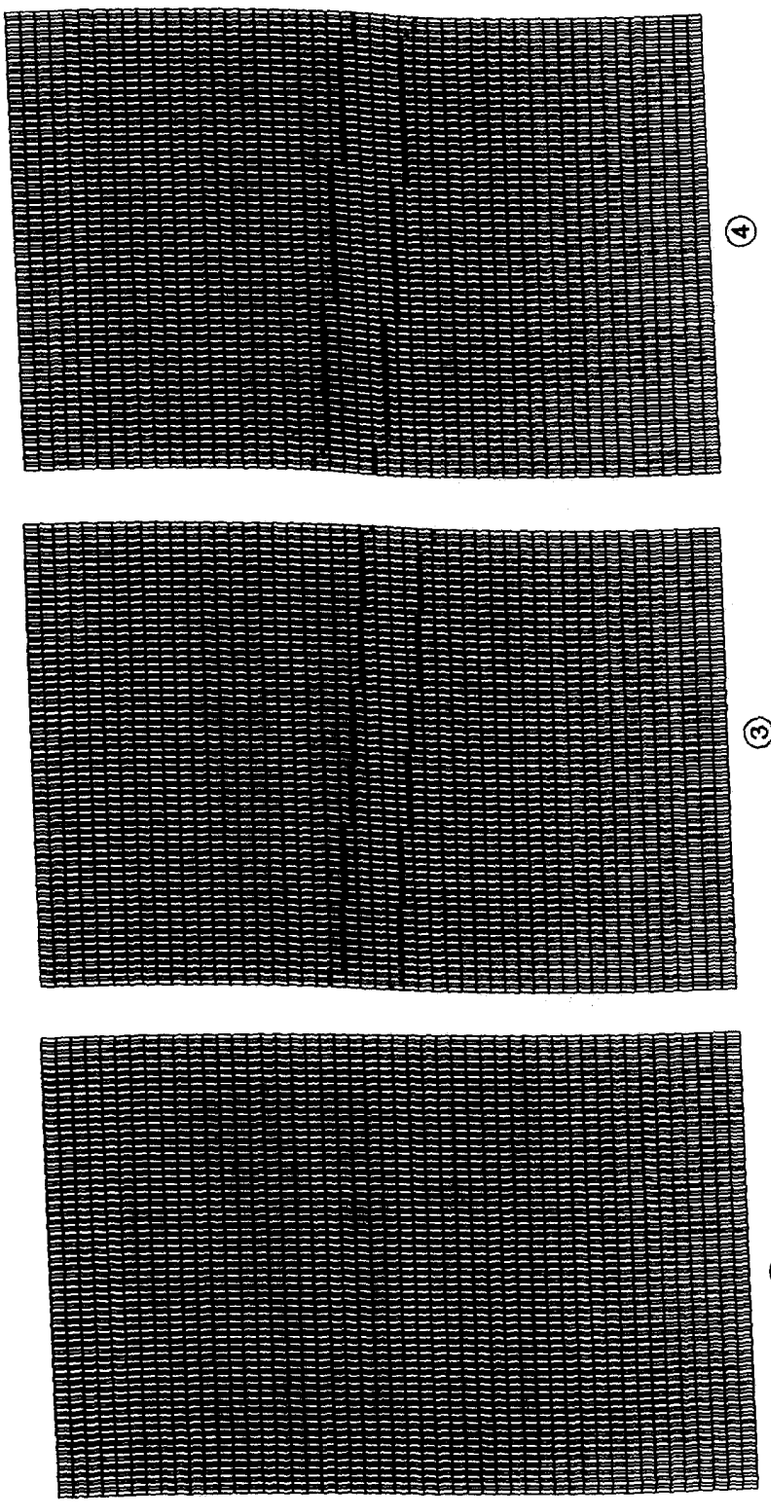

Fig. 17. The initial and five deformed configurations for microsection analysed in Fig. 16.

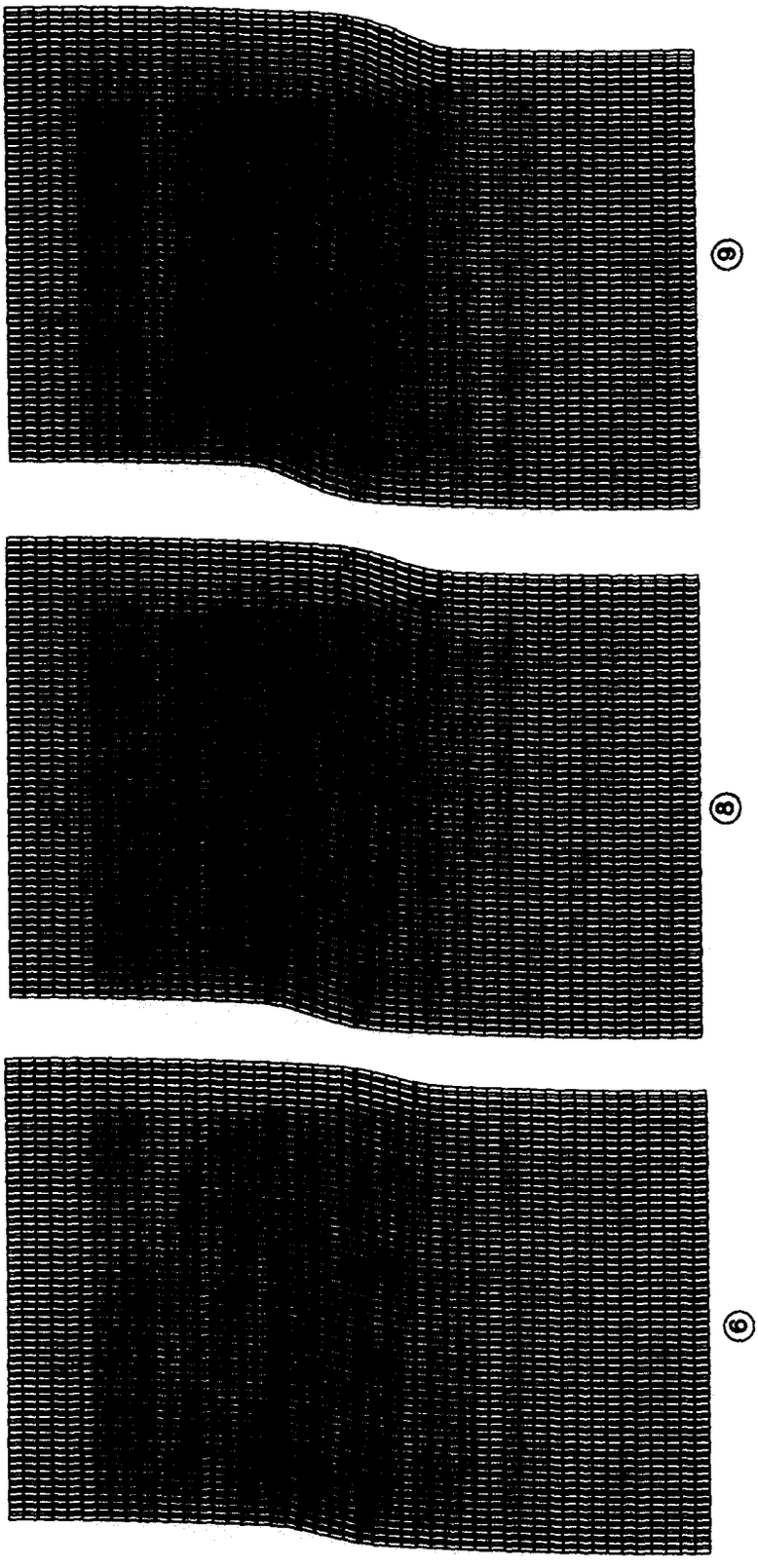

Fig. 17—*continued.*

widths and orientations (the black dots marked on the deformed configurations represent the positions of maximum moments in the fibers). Beyond the limit load, as we progress down the response, in this band the shear connection provided to the fibers by the matrix degrades considerably. The matrix shears significantly, and the fibers undergo significant bending. Because the axial stress is decreasing, away from this highly deformed band, the composite unloads elastically. In the case shown, the specimen is long enough such that the axial deformation recovered from the section away from the highly deformed band is initially much higher than the axial shortening in the band. The net result is elongation of the specimen. This causes the cusp-like response exhibited after the limit load [see Kyriakides (1993) for a number of other examples of such behavior). Beyond point ⑥ the deformation in the band is much more than that recovered from the rest of the specimen and, as a result, it dominates the response. [A finite element analysis of a similarly imperfect composite microsection was reported by Guynn *et al.* (1992). They assumed the deformation to remain sinusoidal and, as a result, the localization of deformation following the limit load was suppressed, although limit stresses and strains predicted by such a model would be comparable to the results presented here. Unfortunately, the predicted initial stiffness of their microsection was much lower than that of the APC-2/AS4 composites they modeled, and the predicted critical strains were high due to the very low value of E_{f1} that was used in their calculations.]

The maximum compressive and tensile fiber stresses plotted in Figs 16(b) and (c), respectively, are quite revealing about the possible cause of failure. Up to point ④ no tensile stresses are observed. The applied compressive stress is higher than the tensile component of the bending stresses. The stress concentrations at the two free surfaces on the left and right increase but still decay within a few fibers from the free end. As fiber bending in the highly deformed band increases, tensile stresses develop in the fibers which are seen to progressively grow to very substantial values for points ⑤–⑨ on the response. In addition, the maximum values of the compressive as well as the tensile stresses are seen to vary to some degree across the specimen width. For example, at point ⑥, the maximum tensile stress is of the order of 200 ksi (1.38 GPa), and the maximum compressive stress is of the order of 450 ksi (3.1 GPa). At point ⑦ the maximum tensile stress has reached 300 ksi (2.07 GPa) and the maximum compressive stress has exceeded 500 ksi (3.45 GPa). The corresponding values at point ⑨ reach levels of more than 500 and 800 ksi (3.45 and 5.5 GPa), respectively. If the deformation of the specimen is continued past this point the tensile stresses grow to even higher values.

The tensile strength of AS4 fibers is quoted [manufacturer specifications; see also Donnet and Bansal (1990)] to range from 300 to 800 ksi (2.1 to 5.5 GPa); in contrast, the tensile strength of the fibers, back calculated from a tensile test on the composite, is approximately 500 ksi (3.45 GPa). Information on the compressive strength of fibers is even less precise but it is expected to be higher than the tensile strength. (Ideally, what is required for the purposes of this analysis is the bending strength of fibers embedded in a matrix. Results from single fibers may not be representative of the strength of fibers in a composite.) Thus, it is difficult at this stage to pinpoint the onset of failure on the response. In spite of this, it can be concluded from the evidence presented that the specimen analysed will fail due to fiber bending somewhere beyond point ⑥ [Fleck *et al.* (1993) reached a similar conclusion following an alternate method of analysis].

A detailed examination of the evolution of the highly deformed band in the middle of the microsection analysed is worthwhile. As in other plastic buckling problems, localization of deformation starts immediately after the limit load. By configuration ③ in Fig. 17(a), localization is seen to take the form of a distinct band of higher deformation. The band is oriented at approximately 7.2° to the x_2-axis of the material (henceforth called angle β) and has a width (w) of approximately 13 fiber diameters ($13h$). The band becomes more distinct in configurations ④ and ⑥ although these geometric characteristics do not change significantly. However, by configuration ⑧, $\beta \approx 10.8°$ and $w \approx 19h$, and in configuration ⑨, $\beta \approx 11.7°$ and $w \approx 23h$. The fibers in these bands are still intact and thus one-to-one comparison with the orientations and widths of the kink planes measured is somewhat unfair. However, it is interesting to observe that both the orientations, as well as the widths

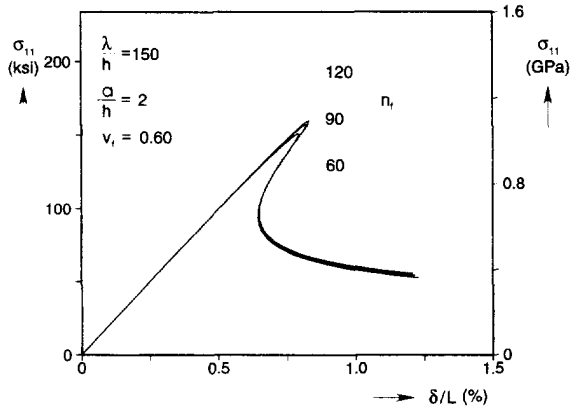

Fig. 18. Comparison of axial stress–end shortening responses of microsections with different widths.

of the bands in the last two configurations in Fig. 17(b), are quite close to the corresponding values measured in the kink planes. This provides further support to the failure scenario described above that the kink planes seen in failed composite specimens are the result of localization of deformation after the limit load. Since the maximum fiber bending stresses occur at the boundaries of this band, failure can be expected to start at the free surfaces. Even though the sequence of events that would follow the progressive breaking of fibers cannot be predicted from the present results, it is reasonable to conjecture that the orientation of these bands is related to the kink band angles seen in the experiments.

3.1.1. *Effect of microsection width.* The specimen analysed has free vertical edges. It has already been demonstrated that stress concentrations develop at these edges. Thus, it is instructive to examine how these edge effects affect the compressive response of microsections with different widths. To this end, microsections with the same imperfection parameters as those of the case in Fig. 16 ($\lambda = 150h$, $a = 2h$), but 90 and 150 fibers wide were compressed in the same fashion as described above. The σ_{11}–δ responses of the three microsections are compared in Fig. 18. The responses are very similar except that, as the specimen becomes wider, the critical stress increases somewhat (see also Table 3). Thus, as expected, the effect of the free ends on the critical stress becomes less pronounced as the specimen becomes wider.

The angles and the widths of the highly deformed bands in these three specimens at an average strain of 1.2% are listed in Table 3. As can be seen both remain relatively unaffected by the specimen width. (Note that due to the symmetries assumed at the top and bottom of the microsection, for any chosen value of λ, there exists a limiting value of microsection width beyond which the highly deformed band starts to be constrained by these symmetries. Beyond this critical width, at any selected value of average axial strain, β decreases as n_f increases.)

Table 3. Comparison of critical stresses, band angles and widths for microsections of three different widths

$\frac{\lambda}{h}$	$\frac{a}{h}$	$\frac{\lambda}{a}$	n_f	$\frac{w}{h}$	β^0	σ_C ksi (GPa)
150	2	75	60	23	11.7	151 (1.04)
150	2	75	90	22	11.7	157 (1.08)
150	2	75	150	25	10.9	160 (1.10)

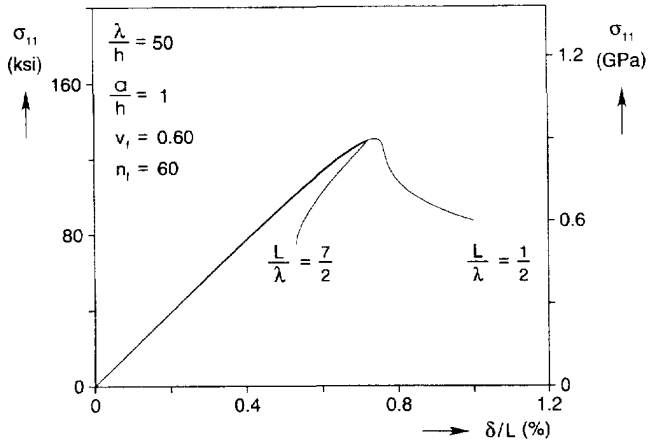

Fig. 19. Comparison of axial stress–end shortening responses from microsections of different length but with the same imperfections.

3.1.2. *Effect of microsection height.* The sharpness of the cusp-like unloading response depends on the height of the specimen analysed. For example, the response of a microsection one third as tall as the one in Fig. 16 ($L = \lambda/2$, $\lambda = 50h$ and $a = h$), shown in Fig. 19, exhibits no cusp and the end shortening monotonically increases. The width of the highly deformed band can be seen in Fig. 20 to be of the same order as that of the longer specimen shown. Thus, the length of the section of this specimen which unloads elastically is significantly shorter, and the shortening in the highly deformed band overwhelms the lengthening contributed from the part that unloads.

In these analyses we assumed that the initial imperfection varies sinusoidally along the fiber direction and that the deformed patterns in Figs 17 and 20 repeat every half a wavelength. As was discussed in the experimental section, in actual composites the amplitude of fiber imperfections varies with position. One of the effects of such variations can be illustrated by considering a microsection with the following imperfection

$$v_0 = \left[a + a_1 \cos\frac{\pi x_1}{n\lambda}\right]\cos\frac{\pi x_1}{\lambda}. \tag{6}$$

We arbitrarily select $n = 7/2$, $a_1 = 0.1h$ and leave all other problem variables the same as those given in Fig. 19. The $\sigma_{11}-\delta$ response of this microsection is compared to that from

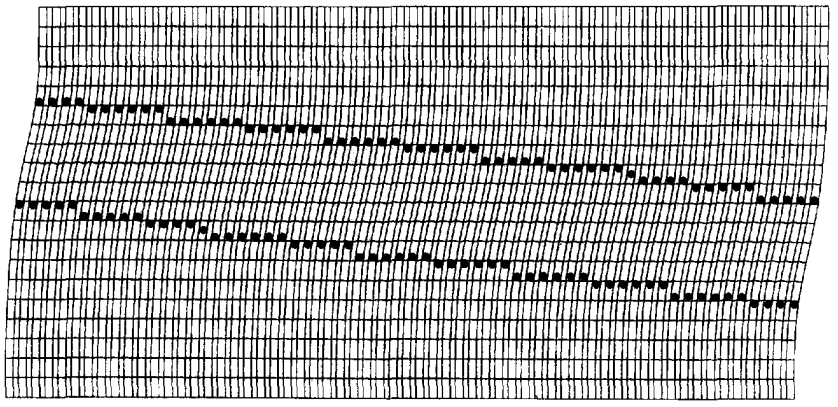

Fig. 20. A deformed configuration from specimen with length of $\lambda/2$.

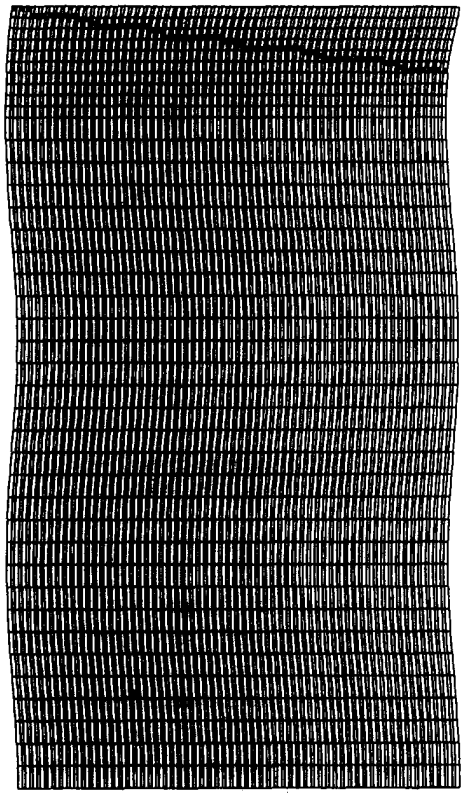

Fig. 21. A deformed configuration for specimen with length of $7\lambda/2$.

the shorter specimen in Fig. 19. A deformed configuration of this case is shown in Fig. 21. The two responses are almost identical up to the limit load [the small difference in the limit loads is due to the somewhat larger imperfection amplitude at $x_1 = 0$ implied by eqn (6)]. After the limit load, the deformation localizes in a band of similar dimensions as the one in the specimen in Fig. 20. However, the length of the section of the specimen which unloads after the limit load is somewhat larger than 3λ. As a result, the σ_{11}–δ response exhibits a very significant cusp (see Fig. 19).

The results presented above illustrate the highly unstable nature of this type of composite. However, the quasi-static responses calculated are, almost certainly, unattainable in practice for the following reasons. In a typical experiment, the specimen will be significantly longer than the lengths of the microsections analysed and, as a result, at the limit load they will have stored significantly higher levels of energy. The cusp-like unloading response will be even sharper than the one shown in Fig. 19. Thus, even under displacement controlled loading, on reaching the limit load, the specimen will snap dynamically, bridging the cusp. The kinetic energy will be provided by the unloading of the specimen. During this dynamic localization process, the fibers in the highly deformed band can be expected to develop bending stresses that are high enough to cause the type of failure shown in Fig. 11.

3.1.3. *Effect of fiber nonlinearity*. In producing the results presented above, the fibers were assumed to be linearly elastic. In reality, they are elastic but somewhat nonlinear (see Fig. A6). The effect of this nonlinearity on the calculated response of microsections, such as the ones described above, was evaluated by idealizing the fiber as a J_2 deformation theory solid. Figure 22 shows a comparison between two axial stress–axial shortening responses of a particular microsection. In the first, the fibers are assumed to be linearly elastic, and in the second they are taken to be nonlinearly elastic with the properties given in Table 1(b). The responses are similar in nature in that they have approximately the same critical stresses (nonlinear fiber 1.3% lower), but the strain at the limit load for the case with the nonlinear fibers is 12% higher than that of the specimen with linear fibers. If the imperfection

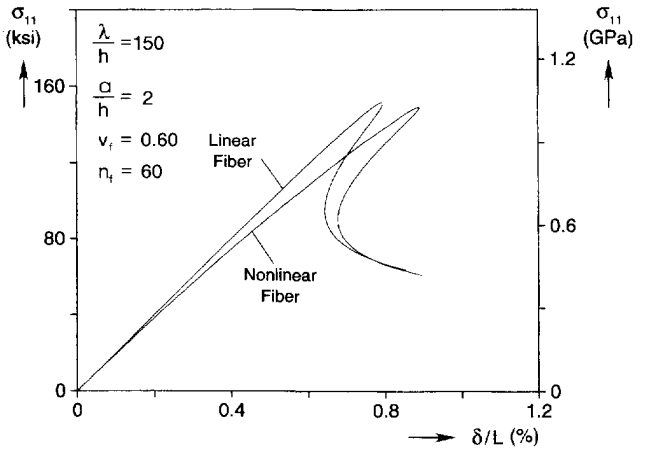

Fig. 22. Comparison of axial stress–end shortening responses for specimens with linearly elastic and nonlinearly elastic fibers.

is smaller, the difference in the critical strains becomes larger but the critical stresses remain approximately the same. Thus, we conclude that the fiber nonlinearity does not alter the failure mechanism and can be neglected in the case of analyses which are conducted for qualitative understanding of the mechanisms governing the problem. However, fiber nonlinearity must be included for quantitative comparisons between measured and predicted critical strains and composite moduli. In the remainder of this paper, unless otherwise stated, the fibers will be assumed to be linearly elastic.

3.1.4. *Effect of imperfection parameters.* The effects of the amplitude and wavelength of fiber imperfections on the response and critical conditions of composite microsegments are illustrated in Fig. 23. Figure 23(a) shows σ_{11}–δ responses for specimens with the same imperfection amplitude ($a = h$) and three different wavelengths. An increase of the wavelength results in a stiffer response and a higher limit load. Figure 23(b) shows similar results for fiber imperfections with fixed wavelength ($\lambda = 150h$) and three different amplitudes. Increasing the amplitude reduces the stiffness of the material as well as its strength. The limit stresses and strains for these cases are given in Table 4. It is interesting to observe that, in all cases shown, the values of the critical stresses are in the same range as those of the critical stresses measured in the experiments. However, this is partly due to the fact that the imperfection parameters considered here do not fully cover the full range of the measured parameters which were reported in the experimental section of this paper. It is clear that a quantitative comparison between experiments and analysis will require a more refined representation of the measured imperfections.

Previous investigators have represented fiber imperfections with just one parameter, the fiber misalignment angle θ_0 [e.g. eqn (4)]. For longer sinusoidal imperfections, this can be approximated by the maximum misalignment angle in the fibers, that is,

$$\theta_0 \approx \frac{\pi a}{\lambda}. \tag{7}$$

Figure 23(c) shows a set of responses in which the maximum misalignment angle was kept constant by prescribing $\lambda = 50a$ and varying the imperfection wavelength. We observe that the limit loads vary with λ even though the variation could perhaps be viewed as a second order effect.

A similar exercise was conducted for $\lambda/a = 75$ which corresponds to the case presented in Fig. 16. Specimens with $\lambda/h = 100$, 150 and 250 were analysed. The critical stresses calculated, as well as the band orientations and widths at an average strain of approximately 1.2%, are listed in Table 5. The variation in the critical stresses is again relatively small. The values of β and w in the three cases are quite close. Thus, these values seem to be

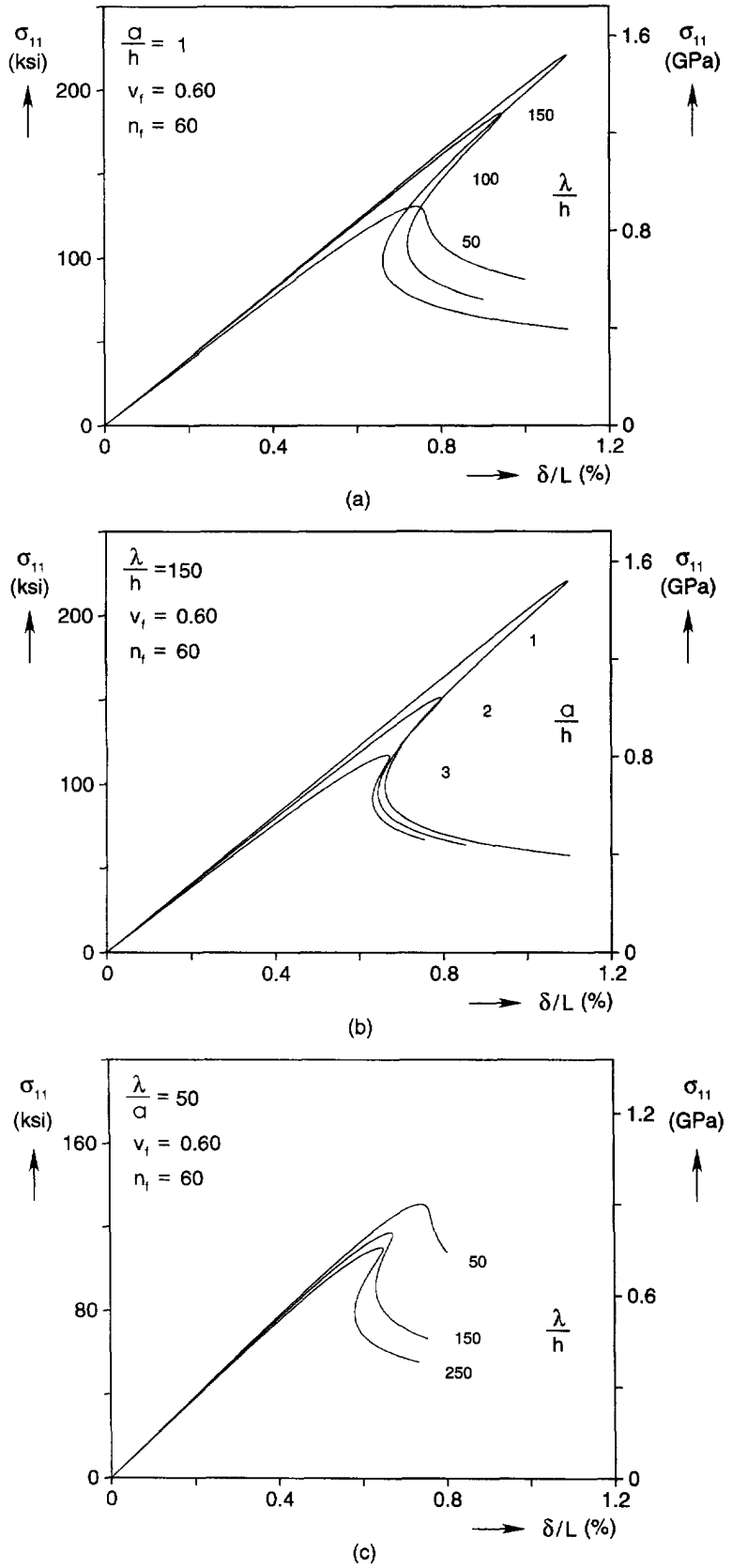

Fig. 23. Axial stress–end shortening responses of specimens with uniformly distributed imperfections: (a) responses for three imperfection wavelengths and $a = h$; (b) responses for three imperfection amplitudes and $\lambda = 150h$; (c) responses for three imperfection wavelengths with $\lambda = 50a$.

Table 4. Critical stresses and strains for micro-segments with uniform imperfections of various amplitudes and wavelengths

$\frac{\lambda}{h}$	$\frac{a}{h}$	σ_C ksi (GPa)	ε_C%
50	1	131 (0.901)	0.741
100	1	186 (1.28)	0.944
150	1	221 (1.52)	1.096
150	2	151 (1.04)	0.793
150	3	117 (0.808)	0.666

Table 5. Comparison of critical stresses, band angles and widths for microsections with three different heights

$\frac{\lambda}{h}$	$\frac{a}{h}$	$\frac{\lambda}{a}$	n_f	$\frac{w}{h}$	β^0	σ_C ksi (GPa)
100	4/3	75	60	20	10.7	157 (1.08)
150	2	75	60	23	11.6	151 (1.04)
250	10/3	75	60	27	11.6	141 (0.97)

relatively insensitive to the specimen height. In view of the similar insensitivity reported earlier when variations in the specimen width were considered, we can conclude that the values of β and w are relatively insensitive to the specimen size.

3.2. *Sinusoidal imperfections with variable amplitude*

In the experimental phase of this study we observed that fiber imperfections, at least in two thermoplastic composites, have non-uniform distributions. For the APC-2/AS4 composite used in the experiments, imperfections in the plane of the prepreg were found to be concentrated in bands of characteristic widths which had a particular periodic distribution in the x_2-direction. Fibers in these bands were distinctly more wavy than in the rest of the composite. In addition, the resin content in these bands was higher than in the bulk material.

Motivated by these observations, in this section, we will analyse the effect of such imperfection non-uniformities on the compressive strength of the material. The purpose of these analyses will be the qualitative understanding of the mechanisms involved. Thus, for computational expedience, but without loss of the generality of the conclusions drawn from the results generated, we will use a specimen with $\lambda = 50h$ and $a = 3h$.

3.2.1. *Centrally located imperfections with decaying amplitude in the* x_2*-direction.*

(i) *Constant matrix volume fraction.* The first case we will examine involves a specimen with a centrally located imperfection and the following spatial distribution

$$v_0 = a\cos\frac{\pi x_1}{\lambda}\exp\left[-\zeta\left(\frac{2x_2}{\alpha b}\right)^2\right] \tag{8a}$$

where b is the width of the microsection, the coordinate x_2 is measured from mid-width,

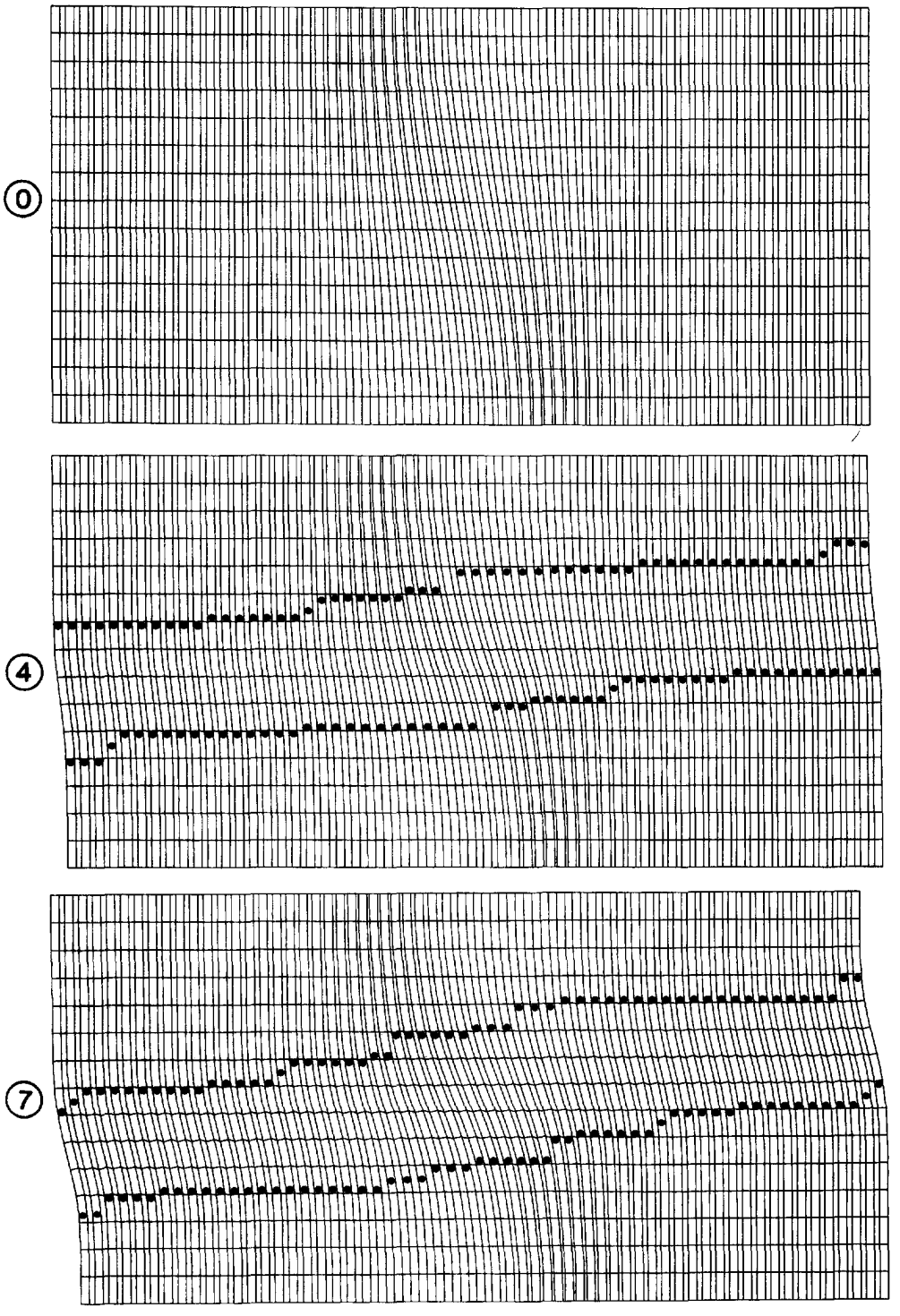

Fig. 24. The initial and two deformed configurations for microsection analysed in Fig. 25.

$$\zeta = \ln(0.01) \quad \text{and} \quad \alpha > 0. \tag{8b}$$

The initial configuration of a microsection with such an imperfection is shown in Fig. 24 (⓪). The microsection is 59 fibers wide. The imperfection has a maximum amplitude of $a = 3h$ which occurs at the center of the specimen. The imperfection amplitude decays to 1% of this maximum value in a width of 14 fibers on either side of the central one. The remaining 15 fibers in each half width are straight. The matrix volume fraction of the

section with the perfectly aligned fibers is 0.40. In the imperfect section, the average matrix volume fraction is also 0.40, but its distribution in the x_1-direction is uneven (see undeformed configuration in Fig. 24). The geometry of the specimen is antisymmetric about the line $x_2 = 0$. We assumed that this antisymmetry is maintained at all stages of deformation; consequently, we analyse only half of the microsection shown in Fig. 24.

The compressive stress–axial shortening response of this microsection is shown in Fig. 25(a). It has the same general characteristics as the corresponding responses of microsections with uniform imperfections. However, this microsection is much stiffer and stronger than the corresponding one with a uniform imperfection with the same wavelength and amplitude. (The specimen with non-uniform imperfection has $\sigma_C = 195$ ksi (1.35 GPa) and $\varepsilon_C = 1.01\%$; the one with uniform imperfection has $\sigma_C = 61$ ksi (42.2 GPa) and $\varepsilon_C = 0.68\%$.)

The maximum compressive and tensile stresses that develop in the fibers at different points along this response are shown in Figs 25(b) and (c). Two deformed configurations of the microsection corresponding to points on the response after the limit load (④ and ⑦) are included in Fig. 24. The deformation again localized to a band, which in configuration ⑦ in the central part of the specimen is approximately $17h$ wide and at the outer edges is approximately $13h$. The band has an inclination of approximately 8°. Initially (points ① and ②), all fibers are in compression and the maximum stresses are quite uniform across the specimen. After the limit load, the compressive stresses become progressively more non-uniform. The matrix in the central part of the specimen undergoes significant shear and its shear stiffness is drastically reduced. The resistance to bending deformation of the central fibers decreases and, as a result, their capacity to carry axial load decreases. Because of this, after the limit load, the compressive axial stress in the central fibers remains relatively unchanged whereas those in the outer fibers increase. After configuration ④, tensile stresses, primarily due to bending, develop in the fibers. The tensile stresses are seen to grow substantially by configuration ⑦. It is interesting to observe that the bending and shearing of the central fibers eventually become so large that, for compatibility with the prescribed symmetry conditions at the top and bottom ends of the microsection, they develop net tensile stresses. This is confirmed by comparing the maximum tensile and compressive stresses in the fibers at ⑦. We can reasonably expect the combination of tensile membrane stresses and bending stresses to eventually lead to fiber failure in the central part of the microsection. Thus, if we assume that the compressive fiber stresses in this microsection can safely be sustained then, in this case, failure will initiate in the middle of the specimen and propagate towards the outer boundaries.

In order to investigate the effect of specimen width on the calculated response of such specimens, the same calculation was repeated for a specimen with 179 fibers, and all other variables kept at the same values ($\alpha = 1/2$). The calculated response was very similar to that in Fig. 25(a). The critical stress and strain increased by less than 1%. The deformation localized in a band which was wider than the ones in Fig. 24, but the orientation was almost the same. At a net shortening of the specimen of approximately 1.2%, the width of the highly deformed band was approximately $20h$ in the center of the specimen and decreased to approximately $13h$ at the outer edges. Its inclination was approximately 7°.

The effect of the parameter α, the ratio of the number of imperfect fibers to that of the total number of fibers in the specimen, is shown in Fig. 26(a). Results for α values of 1/3, 1/2 and 1 are shown. The response of the corresponding microsection with uniform imperfections ($\alpha = \infty$) is also included in this figure. As α increases, the critical stress of the microsection decreases, and the initial stiffness of the composite degrades by some amount. We observe that the three cases with non-uniform distributions of imperfections have significantly higher limit stresses, limit strains, and initial stiffnesses than the one with uniform imperfections. This clearly illustrates that the spatial distribution of imperfections plays a significant role on the critical load of the composite. The widths and orientations of the highly deformed bands, at approximately the same values of δ/L for values of α of 1/3, 1/2 and 1, were found to be approximately the same. By contrast, in the corresponding case with uniform imperfection ($\alpha = \infty$), the inclination of the band was approximately 11° whereas its width was of comparable value to those of the other three cases.

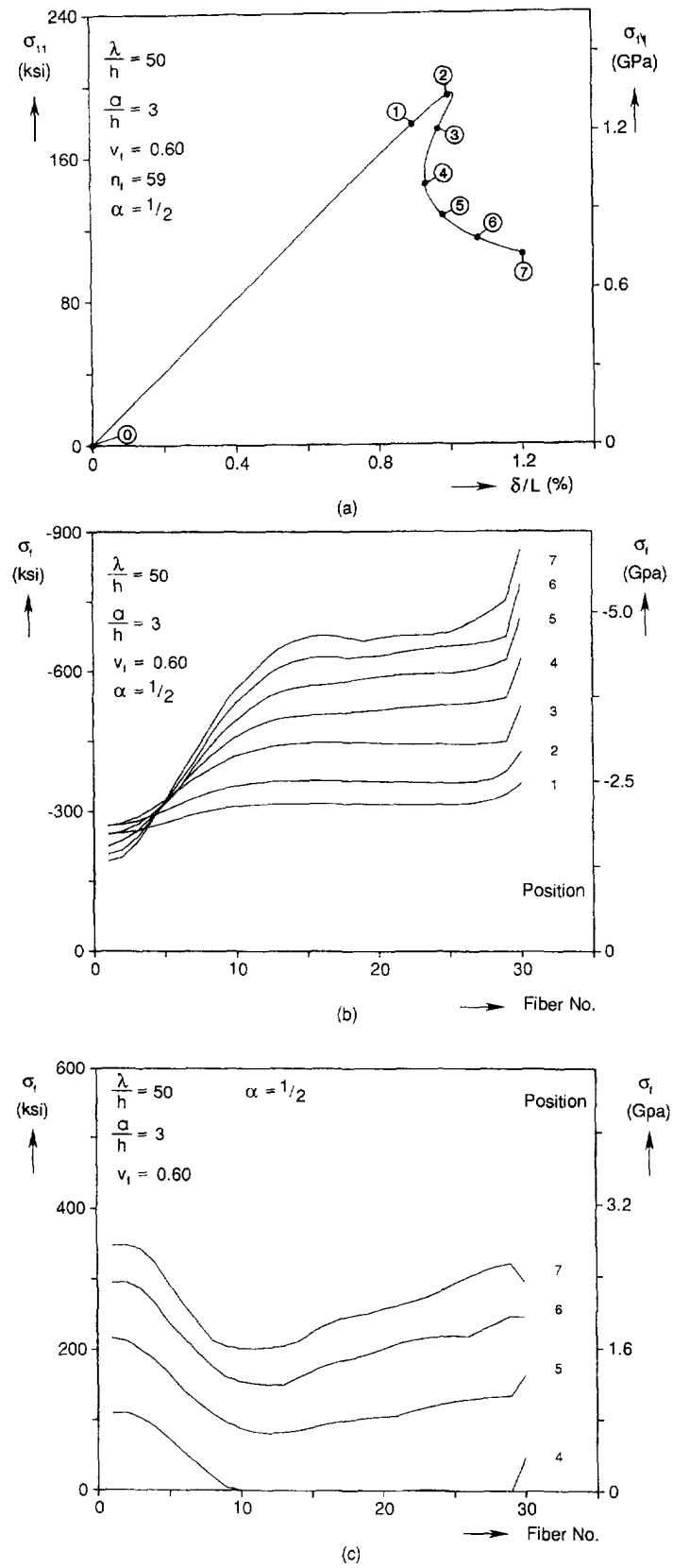

Fig. 25. Analysis of a microsection with centrally located imperfections with decaying amplitude and fixed v_f: (a) axial stress–end shortening response; (b) maximum compressive stresses in fibers at several points on response; (c) maximum tensile stresses in fibers at several points on response.

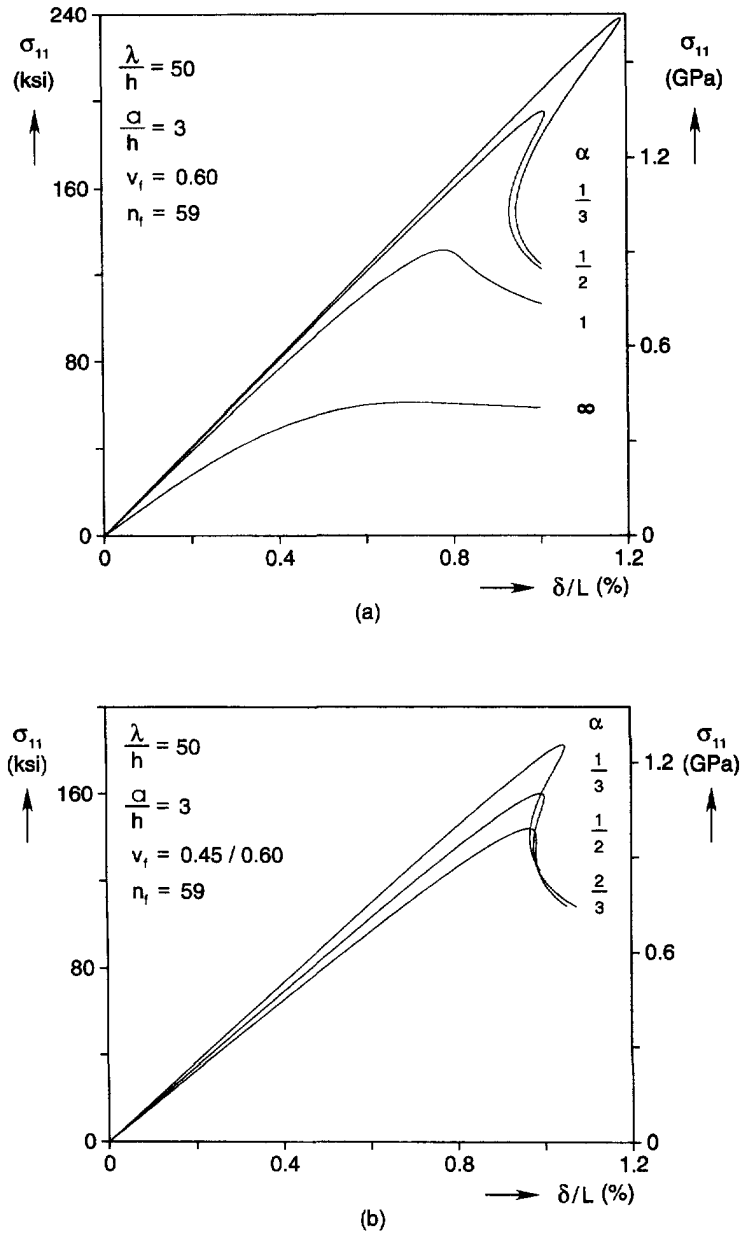

Fig. 26(a). Axial stress–end shortening response for microsections with centrally located imperfections with amplitudes with different domains of decay and fixed v_f; (b) axial stress–end shortening response for microsections with centrally located imperfections with amplitudes with different domains of decay and variable v_f.

(ii) *Variable matrix volume fraction.* Similar calculations were also performed for microsections with imperfections with the same spatial distribution but in which the matrix volume fraction in the imperfect region was assumed to be higher than the nominal value of 0.40. The initial configuration of a representative case in which $v_f = 0.45$ for the inner 29 fibers and 0.60 for the outer 30 fibers is shown in Fig. 27 (see ⓪). The imperfection amplitude is again $a = 3h$ in the center and decays by 99% in the width containing 14 fibers on either side of the central one. The axial stress–end shortening response of this microsection is shown in Fig. 28 together with the maximum compressive and tensile stress distributions in the fibers. Included in Fig. 28(a) is the corresponding response from the case with constant matrix volume fraction [from Fig. 25(a)]. As expected, an increase in the matrix content reduces the initial stiffness of the response and results in a lower limit stress [dropped from 195 ksi (1.35 GPa) for $v_f = 0.60$ to 160 ksi (1.35 GPa) in this case].

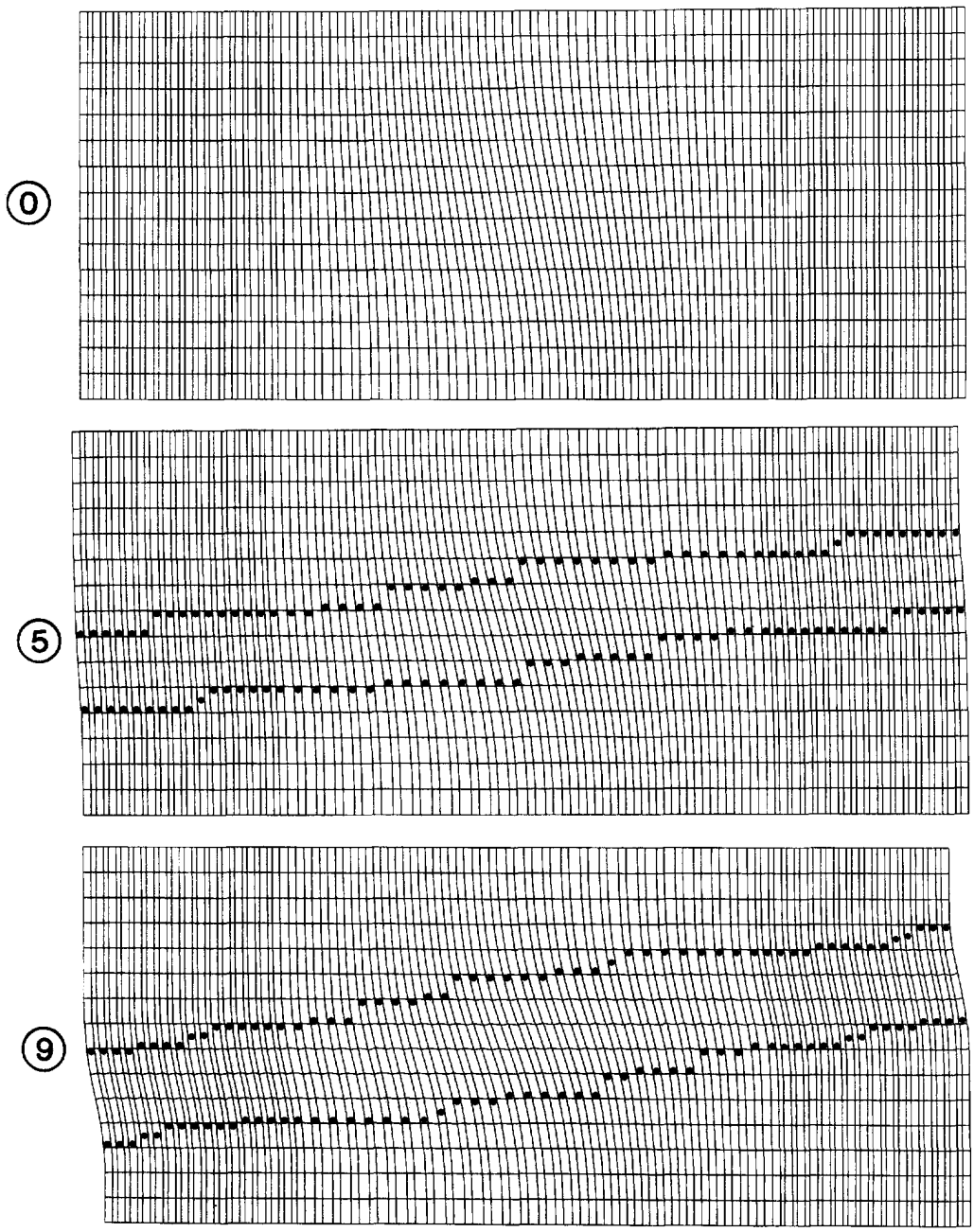

Fig. 27. The initial and two deformed configurations for microsection analysed in Fig. 28.

The main features of the post-limit load behavior of the microsection are qualitatively the same as those for the case with constant v_f. Two deformed configurations corresponding to points ⑤ and ⑨ on the response are shown in Fig. 27. In configuration ⑨, the band width of localized deformation is approximately $16h$ in the central part of the specimen, and its inclination β is approximately 8°. Both of these are approximately the same as those found for the case with constant v_f.

An important effect of the presence of additional matrices in the center of the specimen is that the growth of the tensile stresses is delayed as seen by comparing Figs 28(c) and 25(c). At the same time, the additional matrix in the central part of the specimen allows the fibers in the center to deform more easily. The induced bending and shearing deformations result again in the development of net tensile stresses in the central fibers although

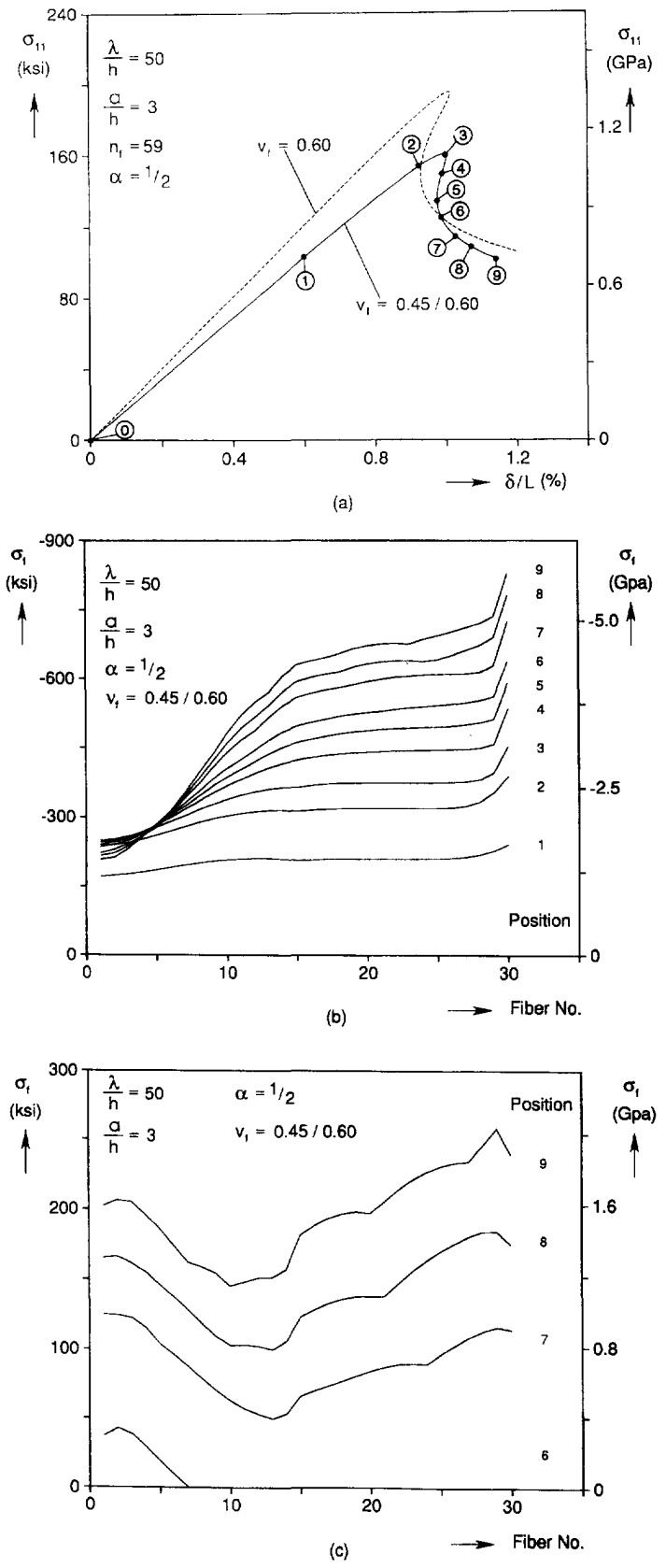

Fig. 28. Analysis of a microsection with centrally located imperfections with decaying amplitude and variable v_f: (a) axial stress–end shortening response; (b) maximum compressive stresses in fibers at several points on response; (c) maximum tensile stresses in fibers at several points on response.

their magnitudes, up to point ⑨ on the response, are smaller than those seen at approximately the same value of δ/L in the corresponding case with constant v_f. Clearly, this specimen is more compliant and will fail at higher values of average axial strain than the case with constant v_f.

Similar calculations were conducted for microsections with the same parameters but with α values of 1/3 and 2/3. The results are compared in Fig. 26(b). As the width of the imperfect central section increases, the initial stiffness of the microsection decreases (primarily due to the increase in the matrix content) and the limit load decreases.

3.2.2. *Edge imperfections with decaying amplitude in the* x_2*-direction.* In all cases presented above, stress concentrations were found to occur at the two free edges of the microsections analysed. This, coupled with the observations of previous investigators that the presence of a free edge can lower the bifurcation stress of aligned composites, indicates that free edges can affect the problem. Motivated by this, we also examined the effect of surface imperfections on the compressive response of our idealized composite. We considered microsections with imperfections with the following spatial distribution

$$v_0 = a\cos\frac{\pi x_1}{\lambda}\exp\left[-\zeta\left(\frac{x_2}{\alpha b}\right)^2\right] \tag{9}$$

where b is the width of the microsection, the coordinate x_2 is measured from the left free edge of the specimen, and ζ and α are as defined in eqn (8b). That is, the imperfection amplitude is maximum at the free edge and decays exponentially for the interior fibers. An example of the initial configuration of such a specimen with $n_f = 60$ is shown in Fig. 29 (⓪). In this case, the amplitude of the imperfection at the free edge is $3h$, and it decays by 99% in the first 30 fibers. The remaining 30 fibers are straight. The matrix volume fraction is kept at 0.40 which again implies that, in the imperfect section, the matrix content varies in the fiber direction.

The axial stress–end shortening response of the specimen in Fig. 29 is shown in Fig. 30. Included in the same figure is the response from a similar microsection with a centrally placed imperfection with the same parameters [taken from Fig. 25(a)]. The two responses are very similar, but the present one exhibits a somewhat reduced initial stiffness and a critical stress which is 2% lower. The distributions of the maximum fiber compressive and tensile stresses are shown in Figs 30(b) and (c), respectively. The values of compressive and tensile stresses are seen to be very comparable to those in Figs 25(b) and (c). In the present case, the maximum fiber bending occurs in the neighborhood of the free end. Again, the deformation induced in the fibers in this region is such that they eventually develop net tensile stresses. By configuration ⑦ the magnitudes of the maximum tensile stresses are again high enough to cause failure of the fibers. However, in this case failure will most probably initiate close to the free edge.

Deformed configurations for points ④ and ⑦ on the response are shown in Fig. 29. As localization progresses, the width and orientation of the highly deformed band are seen to increase. In configuration ⑦ the band has a maximum width of approximately $17h$, and its inclination angle β is approximately 8°. Thus, the band is somewhat wider than that in Fig. 24 which had centrally distributed imperfections. However, the inclinations of the two bands were almost identical.

The same calculation was performed for wider specimens with all other parameters kept the same as those in Fig. 30 ($\alpha = 1/2$). The critical stresses and strains were found to be relatively unaffected by n_f. In addition, the widths and orientations of the highly deformed bands were found to undergo only minor changes with n_f.

Similar calculations were also performed for imperfections with values of α of 1/3, 1 and ∞ and with all other parameters kept at the same values as those of the microsection in Fig. 30. The axial stress–end shortening responses of the four cases are compared in Fig. 31. As was the case for the centrally located imperfections, increases in α reduce the strength of the composite. Again we observe that the initial stiffness as well as the critical stress of

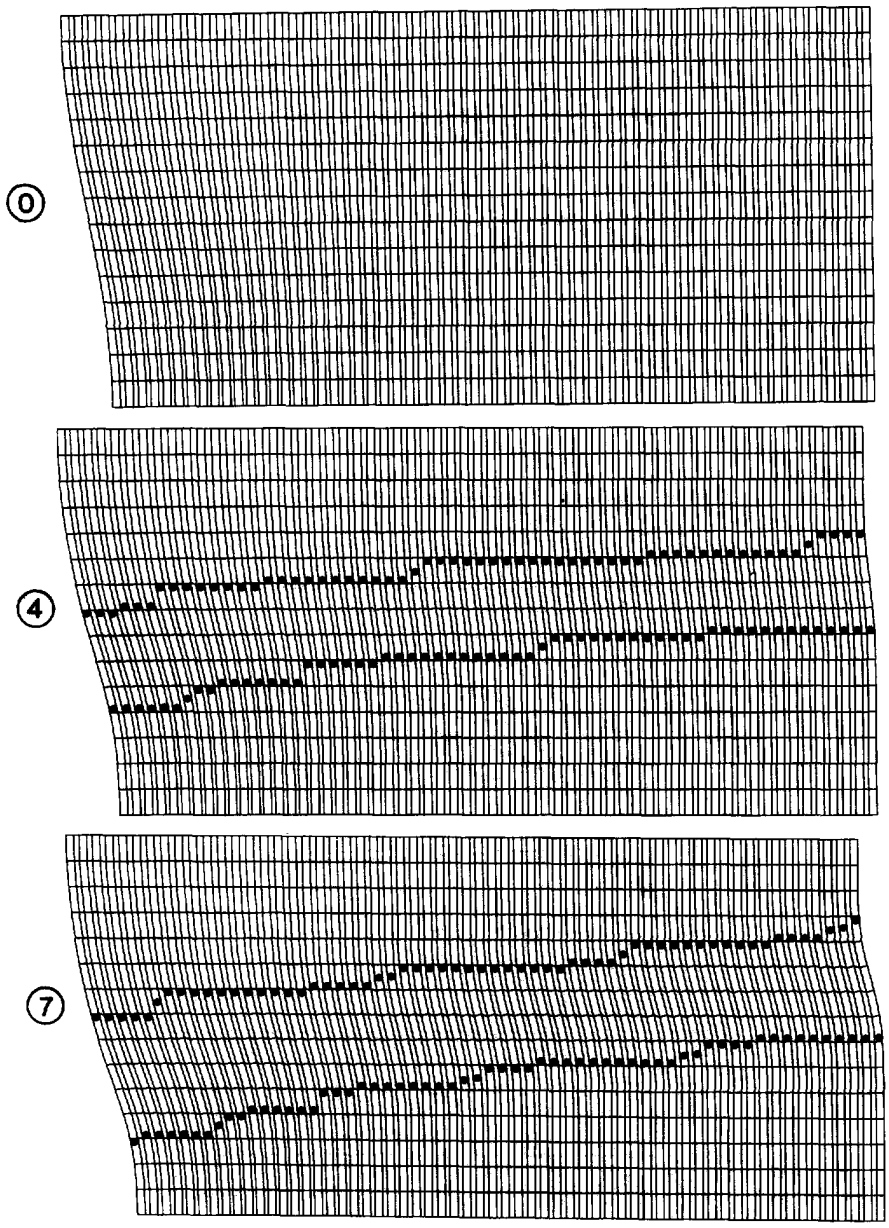

Fig. 29. The initial and two deformed configurations for microsection analysed in Fig. 30.

the case where the imperfection amplitude is uniform through the microsection ($\alpha = \infty$) are much smaller than those of the other specimens.

3.2.3. *Variable amplitude imperfections with* $\lambda = 150$h. In the parametric study of imperfections with variable amplitude presented earlier, the imperfection wavelength was kept constant at $\lambda = 50h$. This value is smaller than the range of wavelengths measured in the APC-2/AS4 composite that was used in the experimental part of this study. The strengths of more representative microsections were also calculated for the following parameters: $\lambda = 150h$, $a = 6h$, $n_f = 79$ and $v_f = 0.60$. The imperfections were centrally located with the spatial distribution given in eqn (8). Microsections with four values of α were analysed. The critical stresses and strains calculated are given in Table 6. The critical stresses for the first three cases are clearly in the range of the values measured in the experiments. The critical strains are somewhat lower than those measured, but this is primarily due to the

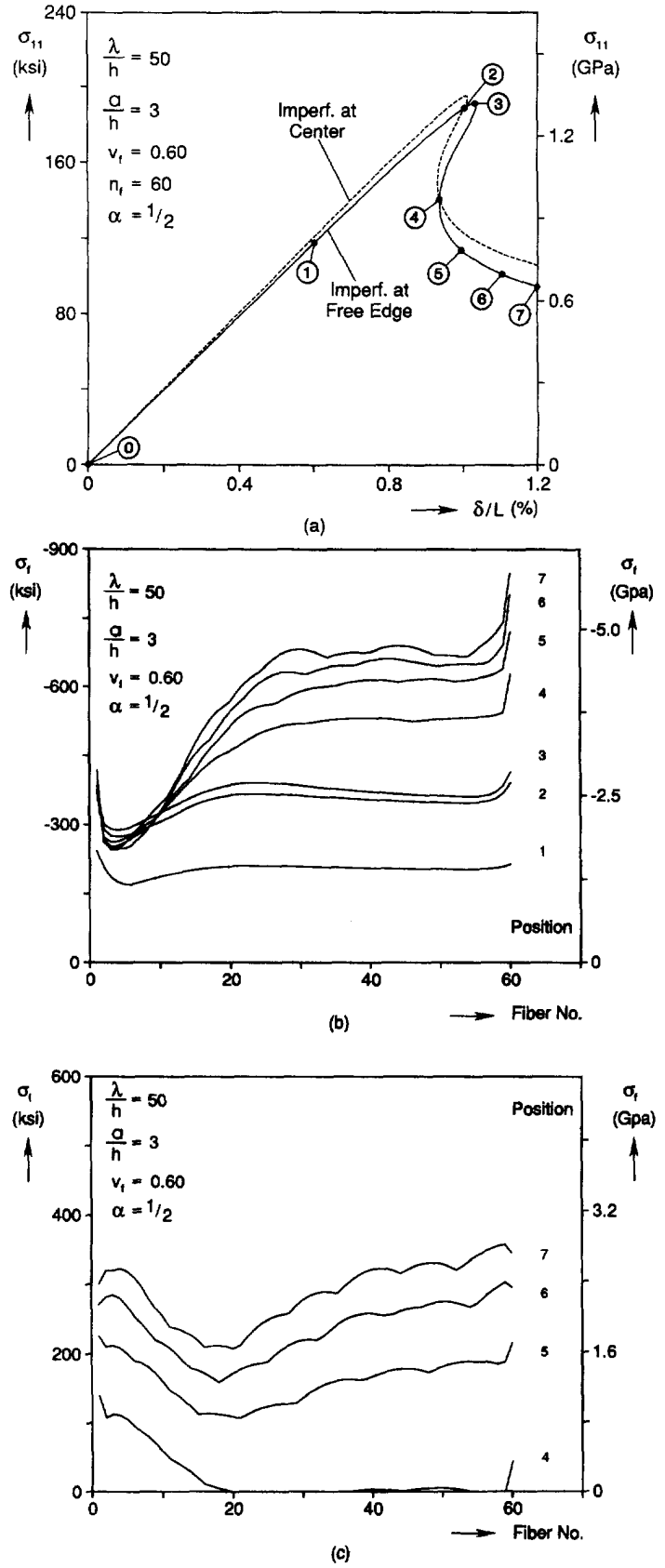

Fig. 30. Analysis of a microsection with imperfections at a free edge with decaying amplitude: (a) axial stress–end shortening response; (b) maximum compressive stresses in fibers at several points on response; (c) maximum tensile stresses in fibers at several points on response.

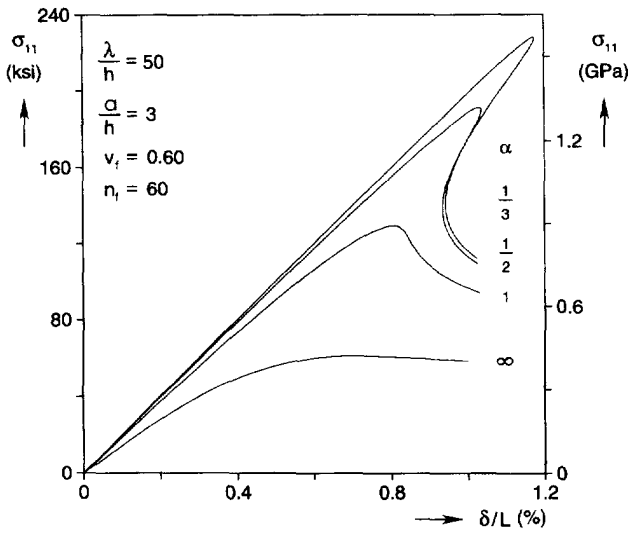

Fig. 31. Axial stress–end shortening response for microsections with imperfections at free edge with amplitudes with different domains of decay.

Table 6. Critical stresses and strains for microsections with imperfections of variable amplitude and $\lambda = 150h$

α	σ_C ksi (GPa)	ε_C%
$\frac{1}{2}$	220 (1.52)	1.06
$\frac{3}{4}$	178 (1.23)	0.88
1	150 (1.03)	0.77
∞	73.1 (0.504)	0.57

fact that the fibers were assumed to be linearly elastic. The case with uniform imperfections with the same amplitude significantly under predicts the experimental values.

A summary of the results for $\alpha = 1$ is shown in Fig. 32. The general characteristics of the results are similar to those presented in Fig. 25 for the shorter wavelength case. In the present case the difference in wavelength and the different spatial distribution of the imperfections result in a different distribution of stresses in the fibers. The maximum tensile and compressive stresses occur at the free edges of the specimen. Thus, failure can be expected to initiate at the free edges and propagate towards the interior. Deformed configurations corresponding to points ④, ⑦ and ⑧ on the response [see Fig. 32(a)] are shown in Fig. 33.

As the process of localization progresses, the highly deformed zone is seen to become wider and its inclination to increase. In each case the band is wider at the center of the specimen. The maximum widths in the three configurations are approximately $17h$, $25h$ and $26h$, respectively. The inclinations of the bands are approximately 7°, 12° and 13°, respectively. These bands are at least a prelude to the kink bands seen in the experiments. If we accept the premise that their geometry is related to that of the kink bands then, clearly, the angles of the bands in the last two configurations, as well as their inclinations, compare very well with those measured. Since both of these change as the localization progresses, the actual failure angle will depend on the strength of the fibers. An accurate value for the strength of AS4 fibers in the setting of this analysis is not available to us at this time, but values in the range 400–500 ksi seem reasonable from the information we have. If we accept that, on reaching such values of stress the fibers in the highly deformed

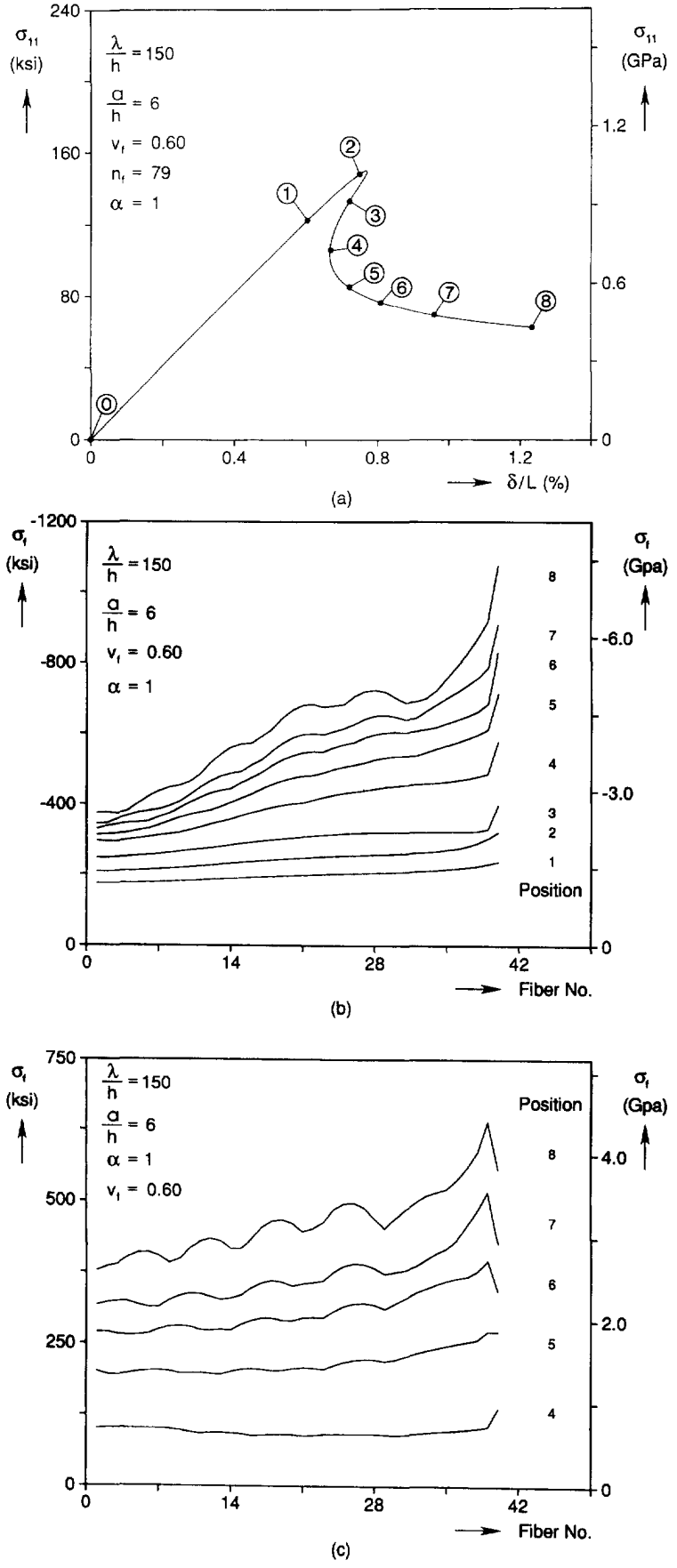

Fig. 32. Analysis of a microsection with $\lambda = 150h$ with centrally located imperfections with decaying amplitude and fixed v_f: (a) axial stress–end shortening response; (b) maximum compressive stresses in fibers at several points on response; (c) maximum tensile stresses in fibers at several points on response.

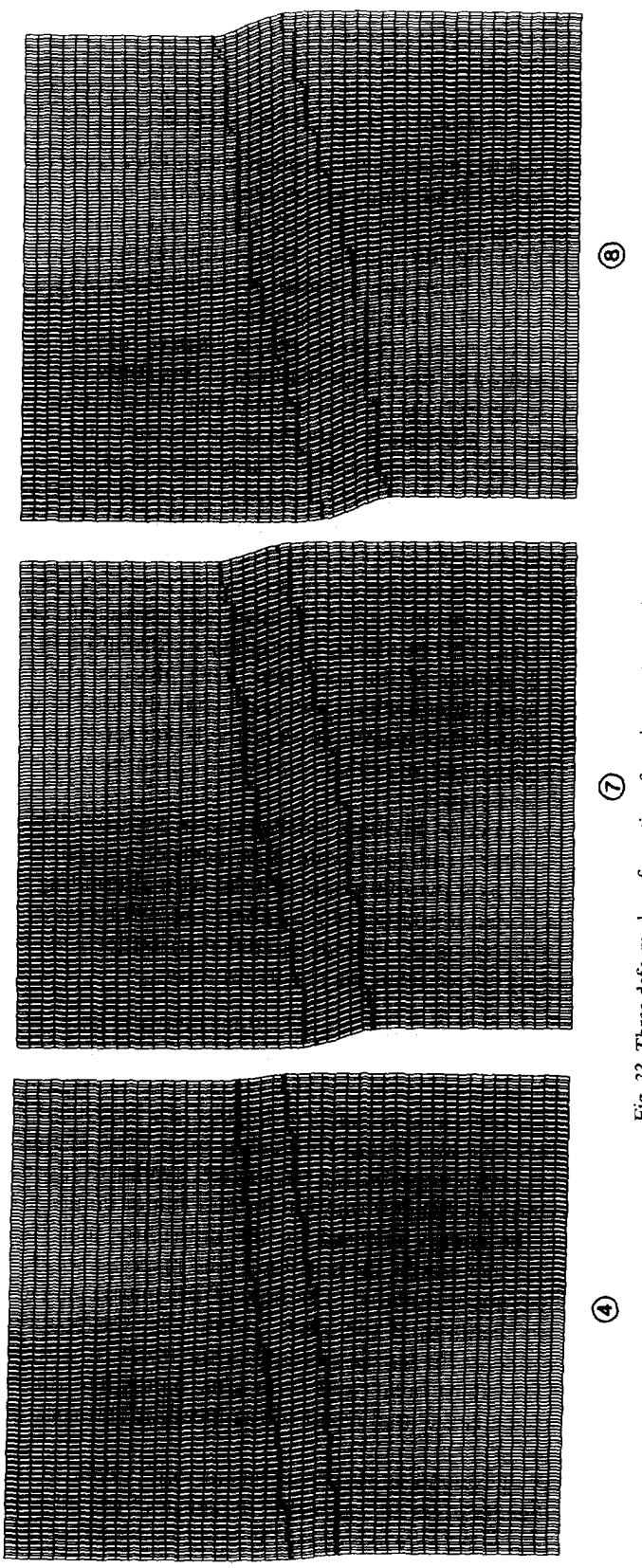

Fig. 33. Three deformed configurations for microsection analysed in Fig. 32.

bands will start breaking by bending, then the formation of the kink band can be expected to occur in the neighborhood of points ⑦ and ⑧ on the response.

4. SUMMARY AND CONCLUSIONS

This paper has addressed the mechanism through which fiber composites fail in compression. Experiments on APC-2/AS4 composite confirmed that previously reported compressive strengths of approximately 175 ksi (1.21 GPa) and corresponding strains of approximately 1.09% are realistic. By contrast, the critical strain predicted by even the most complex analysis in which fibers are assumed to be perfectly aligned and failure is associated with the lowest bifurcation load, is approximately 3%. This difference confirms Argon's argument (1972) that fiber imperfections play a decisive role on the actual strength of such composites. Examination of the composite used in this study revealed some insight as to the nature of such imperfections. It was found that, in addition to imperfections introduced during the curing of a laminate, imperfections were also introduced during the manufacturing of the prepreg of the composite. These imperfections had characteristic periodic spatial distributions. Bounds for their parameters were established.

Experiments on circular rods provided clear and unequivocal evidence that failure of such composites results in kinking of fibers along planes with non-zero inclinations to the x_2-direction of the composite. By confining the region of failure within a steel cavity, it was possible to limit the extent of post-failure deformation in a particular kink plane and to continue loading the specimen. This produced a progressive formation of alternating kink planes within the confined section of the specimen. This process was controllable and occurred at a well defined load plateau which was lower than the load at which failure was initiated in the specimen. Post-failure examination of the failed specimens proved that the kinked fibers failed by bending and provided quantitative information about the widths and inclinations of the kinked planes.

Motivated by the experimental findings, analyses were performed in which the compressive response of representative microsections of an idealized composite were evaluated. The composite was idealized as a two-dimensional solid with alternating fiber and matrix layers, each having the measured properties of AS4 fibers and APC-2 matrix. Microsections of finite width with imperfections of various spatial distributions were analysed. The following conclusions can be drawn from the results produced.

- Compression of such microsections with imperfections activates shear in the matrix. The matrix has limited strength and a highly nonlinear response. As deformation progresses, its shear modulus and, as a result, the overall axial stiffness of the composite are progressively reduced until a limit load is reached. Beyond the limit load, the deformation in all microsections analysed was found to localize in inclined bands of well defined widths. For microsections with imperfection parameters similar to those measured in the experiments, it was found that the deformation in these bands could grow to significant values, driven by just the energy released by the unloading that takes place in the neighboring material. In other words, the post-limit load response was found to be highly unstable, and in essence, uncontrollable. The flow of the matrix in these bands is high and results in significant bending of the fibers. Eventually, the bending stresses reach values that are comparable to the tensile strength of the fibers. It is surmised that when this happens, the fibers start to break and form kink bands like the ones seen in the experiments. Thus, kinking is the final result of the localization process initiated by the limit load instability.
- Aspects of this sequence of events was also described in Steif (1990a, b) and in Yin (1992). Although the present results point to a possible sequence of events which can result in kinking, in a realistic specimen all events past the limit load which affect the formation of the kink bands take place dynamically. The effect of inertia and that of the rate dependence of the matrix to the kinking is not known. However, the calculated response up to the limit load is relatively insensitive to these parameters, and thus the failure loads predicted by the present analyses should be representative.

- The spatial distribution of imperfections was found to affect the response of the composite qualitatively as well as quantitatively. For example, the critical loads of imperfect microsections in which the imperfection amplitude varied across the width, in other words imperfections which resemble to some degree those observed in our composite, were significantly higher than those of imperfections with uniform amplitude. The critical stress obtained by assuming the imperfection to be uniformly distributed in the composite, or its simpler relative implied by eqn (4), will in general provide lower bounds on the strength.
- One of the interesting aspects of the results presented is the demonstration that, in such aligned composites, highly deformed inclined bands develop naturally through a process of localization of deformation following the limit load in the axial load–displacement response. These bands develop immediately after the limit load but their inclinations and widths evolve as the post-limit load response progresses. Their inclinations and widths at average microsection strains of 1–1.2% were found to be comparable to those measured in kink bands in failed specimens. Parametric studies indicated that band orientations and widths are relatively insensitive to the microsection size and to the imperfection amplitude and wavelength. The characteristics of these bands in microsections with spatially varying imperfections were, broadly speaking, similar to those in microsections with uniform sinusoidal imperfections.

Acknowledgments—The financial support of the Office of Naval Research under contract N00014-91-J-4091 is gratefully acknowledged. The assistance of A. E. Ruff in several of the computations conducted is acknowledged with thanks.

REFERENCES

Arcan, M., Hashin, Z. and Voloshin, A. (1978). A method to produce uniform plane stress states with applications to fiber-reinforced materials. *Expl Mech.* **18,** 141–146.

Argon, A. S. (1972). Fracture of composites. In *Treatise on Material Science and Technology* (Edited by H. Herman), Vol. 1, pp. 79–114. Academic Press, New York.

Arseculeratne, R. (1993). The compressive failure of aligned fiber composite materials. M. S. Thesis, Aerospace Engineering, University of Texas at Austin, EMRL Report No. 93/5.

Babich, I. Y. and Guz, A. N. (1992). Stability of fibrous composites. *Appl. Mech. Rev.* **45,** 61–80.

Budiansky, B. (1983). Micromechanics. *Comput. Struct.* **16,** 3–12.

Budiansky, B. and Fleck, N. A. (1993). Compressive failure of fiber composites. *J. Mech. Phys. Solids* **41,** 183–211.

Camponeschi, E. T. (1991). Compression of composite materials: a review. In *Composite Materials Fatigue and Fracture* (Edited by T. K. O'Brien), Vol. 3, pp. 550–578. ASTM STP 1110, Philadelphia.

Chaplin, C. R. (1977). Compressive fracture in unidirectional glass-reinforced plastics. *J. Mater. Sci.* **12,** 347–352.

Chatterjee, S. N. and McLaughlin, P. V. (1979). Inelastic shear instability in composite materials under compression. *Proc. 3rd ASCE Engng Mech. Div. Speciality Conf.* Sept. 17–19, pp. 649–652. University of Texas at Austin.

Crasto, A. S. and Kim, R. Y. (1991). Nonlinear stress–strain behavior in advanced fibers and composites. *Proc. 36th Int. SAMPE Symp.*, San Diego, California, April 15–18, pp. 1649–1663.

Donnet, J.-B. and Bansal, R. C. (1990). *Carbon Fibers.* 2nd Ed., Marcel Decker, New York.

Dow, J. F. and Gruntfest, I. J. (1960). Determination of most needed, potentially possible improvements in materials for ballistic and space vehicles. General Electric Co. Report No. TIS R60SD389.

Evans, A. G. and Adler, W. F. (1978). Kinking as a mode of structural degradation in carbon fiber composites. *Acta Metal.* **26,** 725–738.

Ewins, P. D. and Potter, R. T. (1980). Some observations on the nature of fibre reinforced plastics and the implications for structural design. *Phil. Trans. R. Soc. London* **A294,** 507–517.

Fleck, N. A., Deng, L. and Budiansky, B. (1993). Prediction of kink width in fiber composites. Report MECH-203, Harvard University.

Garala, H. J. (1987). Experimental evaluation of graphite–epoxy composite cylinders subjected to external hydrostatic compressive loading. *Proc. Soc. Expl Mech.*, pp. 948–951.

Geymonat, G., Muller, S. and Triantafyllidis, N. (1993). Homogenization of nonlinearly elastic materials: microscopic bifurcation and macroscopic loss of rank-one convexity. *Arch.* Rational *Mech. Anal.* (in press).

Greszczuk, L. B. (1975). Microbuckling failure of circular fiber-reinforced composites. *AIAA J.* **13,** 1311–1318.

Guynn, E. G., Ochoa, O. O. and Bradley, W. L. (1992). A parametric study of variables that affect fiber microbuckling initiation in composite laminates. Part 1—Analyses. Part 2—Experiments. *J. Compos. Mater.* **26,** 1594–1643.

Hahn, H. T. and Sohi, M. M. (1986). Buckling of fiber bundle embedded in epoxy. *Compos. Sci. Tech.* **27,** 25–41.

Hahn, H. T. and Williams, J. G. (1986). Compression failure mechanisms in unidirectional composites. In *Composite Materials* (Edited by J. M. Whitney), pp. 115–139. 7th Conference, ASTM STP 893, Philadelphia.

Hayashi, T. (1965). On the shear instability of structures caused by compressive load. *Proc. AIAA/RAeS/JSASS Aircraft Design Tech. Meeting.* Los Angeles, CA.

Hill, R. (1950). *The Mathematical Theory of Plasticity*. Oxford University Press, Oxford.
Hutchinson, J. W. (1974). Plastic buckling. In *Advances in Applied Mechanics* (Edited by C.-S. Yih), Vol. 14, pp. 67–144.
Jar, P.-Y., Cantwell, W. J. and Kausch, H. H. (1992). Study of crystal morphology and the deformation behaviour of carbon fibre reinforced PEEK (APC-2). *Compos. Sci. Tech.* **43,** 299–306.
Johnson, D. J. (1987). Structural–property relationships in carbon fibres. *J. Phys. D: Appl. Phys.* **20,** 286–291.
Kim, R. Y. and Crasto, A. S. (1992). A longitudinal compression test for composites using a sandwich specimen. *J. Compos. Mater.* **26,** 1915–1929.
Kim, R. Y. and Tsai, S. W. (1988). A compressive test method for ring specimens. *Proc. 33rd Int. SAMPE Symp. Exhibition, Materials Pathway to the Future*, (Edited by G. Carrillo, E. D. Newell, W. D. Brown and P. Phelan), March 7–10, pp. 1159–1168.
Kyriakides, S. (1993). Propagating instabilities in structures. In *Advances in Applied Mechanics* (Edited by J. W. Hutchinson and T. Y. Wu) Vol. **30,** pp. 67–189. Academic Press, Boston, MA.
Lager, J. R. and June, R. R. (1969). Compressive strength of boron–epoxy composites. *J. Compos. Mater.* **3,** 48–56.
Lagoudas, D. C., Tadjbakhsh, I. and Fare, N. (1991). A new approach to microbuckling of fibrous composites. *ASME J. Appl. Mech.* **58,** 473–479.
Lanir, Y. and Fung, Y. C. B. (1972). Fiber columns under compression. *J. Compos. Mater.* **6,** 387–401.
Maewal, A. (1981). Postbuckling behavior of a periodically laminated medium in compression. *Int. J. Solids Structures* **17,** 335–344.
Pagano, N. J. and Halpin, J. C. (1968). Influence of end constraint in the testing of anisotropic bodies. *J. Compos. Mater.* **2,** 18–31.
Parry, T. V. and Wronski, A. S. (1982). Kinking and compressive failure in uniaxial aligned carbon fibre composite tested under superposed hydrostatic pressure. *J. Mater. Sci.* **17,** 893–900.
Paterson, M. S. and Weiss, L. E. (1966). Experimental deformation and folding of phyllite. *Geol. Soc. Am. Bull.* **77,** 343–374.
Piggott, M. R. (1981). A theoretical framework for the compressive properties of aligned fibre composites. *J. Mater. Sci.* **16,** 2837–2845.
Piggott, J. R. and Harris, B. (1980). Compression strength of carbon, glass and Kevlar-49 fibre reinforced polyester resins. *J. Mater. Sci.* **15,** 2523–2538.
Pindera, M.-J. and Herakovich, C. T. (1986). Shear characterization of unidirectional composites with the off-axis tension test. *Expl Mech.* **26,** 103–112.
Pindera, M.-J., Choksi, G., Hidde, J. S. and Herakovich, C. T. (1987). A methodology for accurate shear characterization of unidirectional composites. *J. Compos. Mater.* **21,** 1164–1184.
Pindera, M.-J., Ifju, P. and Post, D. (1990). Iosipescu shear characterization of polymeric and metal matrix composites. *Expl Mech.* **30,** 101–112.
Rosen, B. W. (1965). Mechanics of composite strengthening. In *Composite Materials*, pp. 37–75. American Society of Metals, Metals Park, OH.
Sadowsky, M. A., Pu, S. L., Hussain, M. A. (1967). Buckling of microfibers. *ASME J. Appl. Mech.* **34,** 1011–1016.
Salama, M. M. (1986). Lightweight materials for deepwater offshore structures. *Proc. Offshore Tech. Conf.* OTC 5185, pp. 297–304. Houston, TX.
Schapery, R. A. (1992). Analysis of local buckling in viscoelastic composites. In *Local Mechanics Concepts for Composite Material Systems* (Edited by J. N. Reddy and K. L. Reifsnider), pp. 229–250. *Proc. IUTAM Symp.*, Blacksburg, VA. Springer-Verlag, Berlin.
Schuerch, H. (1966). Prediction of compressive strength in uniaxial boron fiber–metal matrix composite materials. *AIAA J.* **4,** 102–106.
Steif, P. S. (1990a). A model for kinking in fiber composites—I. Fiber breakage via microbuckling. *Int. J. Solids Structures* **26,** 549–561.
Steif, P. S. (1990b). A model for kinking in fiber composites—II. Kink band formation. *Int. J. Solids Structures* **26,** 563–569.
Sun, C. T. and Chen, J. L. (1989). A simple flow rule for characterizing nonlinear behavior of fiber composites. *J. Compos. Mater.* **23,** 1009–1020.
Tarnopol'skii, Y. M. and Kincis, T. (1985). *Static Test Methods for Composites*, Chapter 3. Translated by G. Lubin, Van Nostrand Reinhold Co.
Triantafyllidis, N. (1993). Private communication.
Triantafyllidis, N. and Maker, B. N. (1985). On the comparison between microscopic and macroscopic instability mechanisms in a class of fiber-reinforced composites. *ASME J. Appl. Mech.* **52,** 794–800.
Waas, A. M., Babcock, C. D. and Knauss, W. G. (1990a). An experimental study of compression failure of fibrous laminated composites in the presence of stress gradients. *Int. J. Solids Structures* **26,** 1071–1098.
Waas, A. M., Babcock, C. D. and Knauss, W. G. (1990b). A mechanical model for elastic fiber microbuckling. *ASME J. Appl. Mech.* **57,** 138–149.
Weaver, C. W. and Williams, J. G. (1975). Deformation of carbon–epoxy composite under hydrostatic pressure. *J. Mater. Sci.* **10,** 1323–1333.
Yin, W.-L. (1992). A new theory on kink band formation. In *Proc. AIAA/ASME/ASCE/AHS/ASC 33rd SDM Conf.*, pp. 3028–3035. Dallas, TX.
Yurgartis, S. W. (1987). Measurement of small angle fiber misalignments in continuous fiber composites. *Compos. Sci. Tech.* **30,** 279–293.
Yurgartis, S. W. and Sternstein, S. S. (1988). A micrographic study of bending failure in five thermoplastic–carbon fibre composite laminates. *J. Mater. Sci.* **23,** 1861–1870.

APPENDIX

In this Appendix, we describe the steps that were taken to extract the stress–strain behavior of the AS4 fiber and the PEEK matrix (*in situ*). These properties were, of course, required for the detailed micromodeling effort,

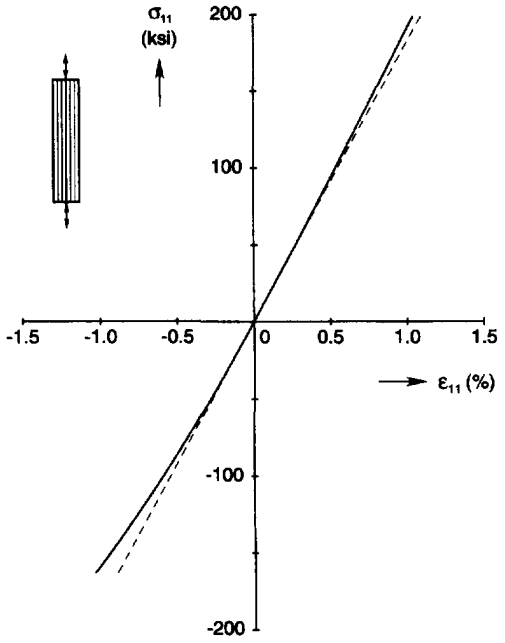

Fig. A1. Measured uniaxial stress–strain response of APC-2/AS4 composite in x_1-direction.

a key point of which was the nonlinear response of the matrix and, to a lesser extent, the fibers. A number of experiments were performed in order to determine the transversely isotropic behavior of the composite. The specimen geometries are shown schematically along with the responses (Figs A1–A3). There was some duplication in the experimental methods used, particularly in shear, in order to remove uncertainties regarding the validity of data obtained from some of the tests.

The response of the composite in the fiber direction was obtained from flat coupons (tension) and rod specimens (compression). The flat coupons had a gage length of 6 in (15.24 cm) and were 0.5 in (12.7 mm) wide by 0.05 in (1.27 mm) thick. They were reinforced at the ends with tapered glass–epoxy tabs that were bonded to the coupons. Axial and transverse strain gages were bonded to the gage section of the specimens using standard procedures. The geometry of the rod specimens and the procedures that were used for the compression tests have been described in the main body of the paper. The measured response in the fiber direction in tension and compression is shown in Fig. A1. The most striking feature is the stiffening behavior in tension and the softening in compression [see also Crasto and Kim (1991)]. It is important to note that this nonlinearity is an elastic feature that results from the lamellar microstructure of the fiber [see Johnson (1987)]. The initial tangent modulus of the composite and the Poisson's ratio are listed in Table 1.

The transverse properties were obtained from two specimen geometries. The tensile response (Fig. A2) was measured with tabbed, flat coupons with a gage section that was 3.3 in (8.38 cm) long by 0.625 in (15.88 mm) wide by 0.10 in (2.54 mm) thick. There was a slight nonlinearity in the response near the maximum stress level. The compressive transverse response was obtained from square cross section specimens with a thickness and width

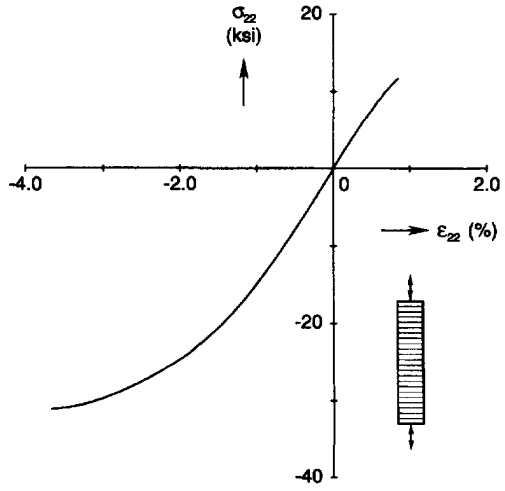

Fig. A2. Measured uniaxial stress–strain response of APC-2/AS4 composite in x_2-direction.

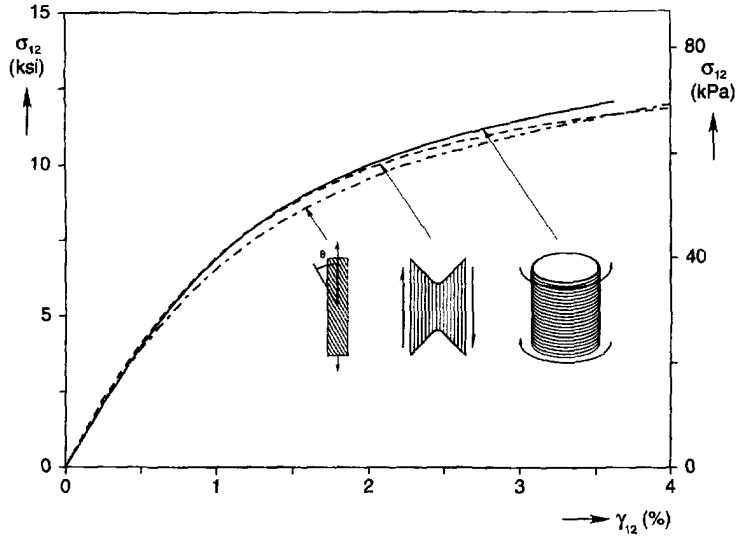

Fig. A3. Measured shear response from three independent tests.

of 0.265 in (6.73 mm) and a length of 3 in (7.62 cm) tested in an aligning device similar to that shown in Fig. 1. The compressive response (Fig. A2) matched the initial tensile modulus but extends to a strain of approximately 4% and is much more striking in its nonlinearity.

The overall shear response of the composite was obtained using the off-axis tension test, the Arcan shear, and torsion of a thin-walled tube as shown schematically in Fig. A3. A specimen with the fibers oriented at 15° to the loading direction was used for the off-axis tension test. Its gage section was 7.7 in (196 mm) long by 0.4 in (10.26 mm) wide by 0.1 in (2.54 mm) thick, giving it an aspect ratio of 19.25 which was large enough to minimize end effects (Pagano and Halpin, 1968; Pindera and Herakovich, 1986). The multiaxial state of stress which develops in the material reference frame can be related to the applied axial stress by simple stress transformation. These stresses, when used in Hill's (1950) anisotropic yield criterion, result in a scalar (equivalent) measure of the state of stress. A strain gage rosette with a 0/30/90° arrangement was used to monitor the strains. An equivalent, incremental plastic strain which is work compatible to the equivalent stress is established from the three measured strain components by assuming that the strain in the fiber direction is strictly elastic (Sun and Chen, 1989). The shear response was evaluated from this equivalent stress–plastic strain response using the classical flow rule of plasticity. The total shear stress–strain response obtained by combining the elastic and plastic strain increments is shown in Fig. A3.

The second configuration that was used to obtain the shear stress–strain behavior of the composite was the Arcan specimen, in the form proposed for composites (Arcan *et al.*, 1978). It had the butterfly shape shown schematically in the inset in Fig. A3 and was bonded to the familiar semi-circular grips using a special alignment jig which was removed just prior to loading. The distance between the grips and the roots of the notches were 0.4 in (10.16 mm) and 0.475 in (12.07 mm), respectively. Since initial measurements with two strain gages placed on either side of the specimen indicated that the mounting procedure did not induce any bending, only one centrally placed shear strain gage was used to measure the strain. The data presented in Fig. A3 was obtained from specimens in which the fibers ran parallel, rather than perpendicular, to the specimen axis that joins the notches.

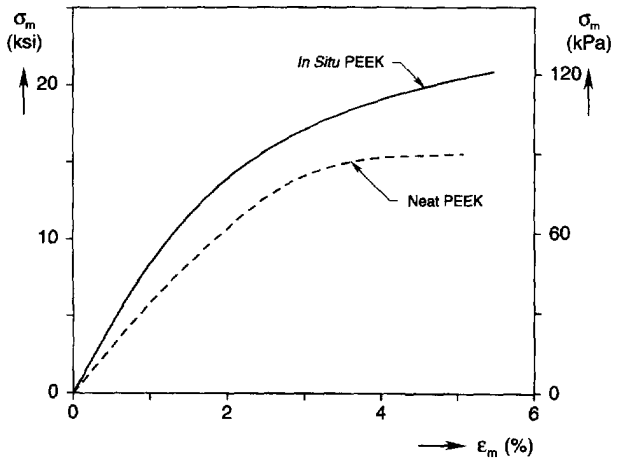

Fig. A4. Comparison of stress–strain response of APC-2 (PEEK) *in situ* and in neat form.

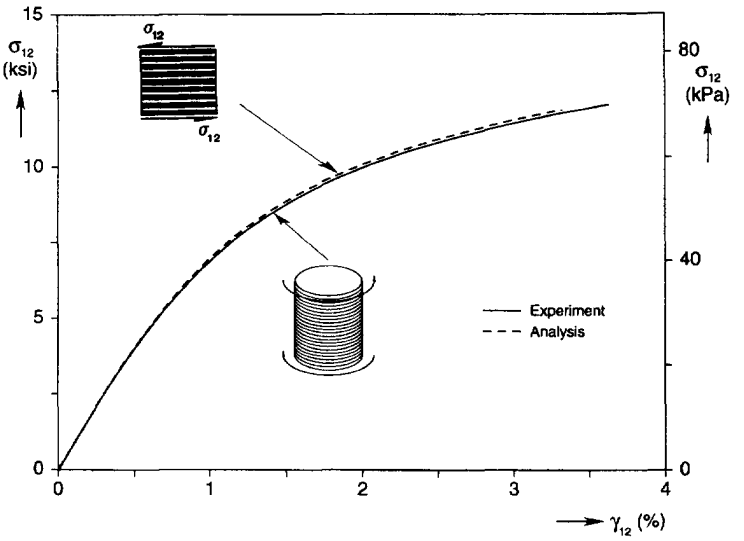

Fig. A5. Comparison of composite shear response measured in the thin-walled tube experiment with that from a numerical simulation of a pure shear test using the properties of the two constituents.

The two possible configurations gave rise to apparently different shear responses, presumably due to the fact that the stress distributions in the two configurations differ, as has been noted in Iosipescu specimens (Pindera *et al.*, 1987, 1990).

The third configuration that was used for measuring the shear response of the composite was a thin-walled tube loaded in torsion. The tube was filament wound in the hoop direction with a mean diameter of 3.096 in (76.8 mm). The outside surface of the specimen was ground in order to provide a uniform wall thickness of 0.090 in (2.29 mm) over the 4.5 in (114.3 mm) gage length. Glass fiber tabs, which were machined to be concentric with the test specimen, were used to reinforce the grip section. The specimen was loaded in an axial/torsional servohydraulic testing facility under rotational control and zero prescribed axial load. Strain gages bonded in the test section were used to measure the shear strain directly.

The three responses are compared in Fig. A3. Taking the tube in torsion as the benchmark, it can be seen that the initial shear moduli obtained from all three specimens were in reasonably good agreement (4.8% and 7.7% higher for off-axis tension and Arcan test, respectively). There were some differences in the responses at higher stress levels, with the upper bound being consistently provided by the thin-walled tube in torsion. The response of the Arcan specimen was closer to that obtained from the tube up to almost 4% shear strain, when stress levels in the Arcan specimen dropped below those obtained from the 15° off-axis specimen. It should be noted that no correction factors were applied to the data obtained from the Arcan experiment. This is in contrast to recent experience with the Iosipescu specimen (Pindera *et al.*, 1987, 1990) where, in specimens with fibers running parallel to the axis, joining the notches resulted in lower stress levels and shear modulus, whereas specimens with fibers perpendicular to the notch axis gave rise to higher stresses and shear modulus.

The next step that was taken was to extract the stress–strain behavior of the matrix and fiber from the shear (Fig. A3) and fiber direction tension/compression (Fig. A1) responses, respectively. The *in situ* axial stress–strain behavior of the matrix (Fig. A4) was derived from the composite shear stress–strain response measured in the tube torsion test using the following steps. The fibers were assumed to be linearly elastic and isotropic with the properties given in Table 1(b), and the matrix was taken to be elastic–plastic. The rule of mixtures was applied incrementally to the elastic and plastic tangent moduli of the shear stress–strain response of the composite to evaluate the shear stress–strain response of the matrix (note that the difference between G_m and G_f is so large that assuming the fiber to be rigid yielded sufficiently accurate results). The axial stress–strain response was obtained from the latter using the customary transformation rules of isotropic elasticity and plasticity. The elastic properties of the matrix are listed in Table 1(c).

The accuracy of these schemes was checked as follows. The shear stress–strain response of PEEK extracted in this fashion was used together with the fiber elastic properties in Table 1 to conduct, numerically, a simple shear test consisting of alternating layers of matrix and fiber materials. The results of this analysis are compared to the measured shear stress–strain response of the composite in Fig. A5. The comparison is very favorable and no further iterations were required.

Included in Fig. A4 for comparison is the stress–strain response of neat PEEK which was measured in separate tests using tensile coupons. It is clear that PEEK in the composite is considerably stiffer and stronger than the neat material. This is due to the formation of transcrystalline regions in the matrix material adjacent to the fibers (Jar *et al.*, 1992).

The stress–strain behavior of the AS4 fibers was obtained in much the same way from the experimental results in Fig. A1. We assumed that the nonlinearity is strictly due to the fiber as opposed to geometric effects. This was supported, to a certain degree, by the fact that loading and unloading in both tension and compression followed the same paths. The result is shown in Fig. A6 where the fibers exhibit stiffening and softening responses in tension and compression, respectively. The compressive part of this stress–strain response was fitted with the three

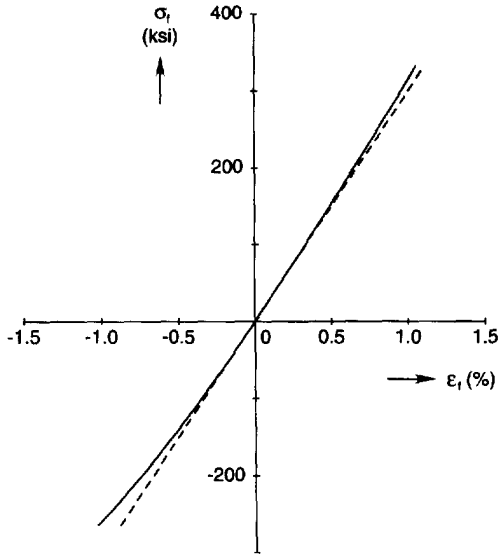

Fig. A6. Fiber uniaxial stress–strain response.

parameter Ramberg–Osgood fit given by

$$\varepsilon = \frac{\sigma}{E_f}\left[1 + \frac{3}{7}\left(\frac{\sigma}{\hat{\sigma}_f}\right)^{n_f - 1}\right].$$

The fit parameters E_f, n_f and $\hat{\sigma}_f$ are listed in Table 1(b).